

## **Interpreting cooling dates and histories from laser ablation in-situ (U-Th-Sm)/He thermochronometry: A modelling perspective.**

Christoph Glotzbach<sup>1</sup>, Todd A. Ehlers<sup>2,1</sup>

5

<sup>1</sup> Department of Geosciences, University of Tuebingen, Tuebingen, 72076, Germany

<sup>2</sup> School of Geographical and Earth Sciences, University of Glasgow, G12 8QQ, UK

10 Corresponding author: christoph.glotzbach@uni-tuebingen.de

### **Abstract**

15

Recent applications of the in-situ (U-Th-Sm)/He thermochronometry technique demonstrate its potential to address some of the analytical challenges associated with the whole-grain technique. In this study, we adapted state-of-the-art apatite and zircon production-ejection-diffusion models for application to in-situ dating methods, aiming to enhance the applicability of this technique to a broad range of geologic samples and applications. Our modifications to thermal history models include accommodation of the full range of stopping distances for alpha particles and cylindrical grain geometries. This investigation focuses on several key aspects of in-situ data interpretation: (i) exploring the relationship between in-situ dates and the position of ablation spots across individual grains, (ii) assessing differences and similarities between whole-grain and in-situ dates, (iii) determining optimal strategies and performance for reconstructing cooling histories from in-situ (U-Th-Sm)/He data, and (iv) reporting the effects of radionuclide zoning on (U-Th-Sm)/He thermochronology. Results indicate that the measured in-situ helium distribution is a function of grain size, ablation spot position and size, and cooling history. Together, these analytical and natural factors result in systematic variations in in-situ dates with distance from the grain rim. Therefore, similar to whole-grain analyses, robust interpretation requires determining grain geometry and the distance of the laser spot to the nearest prismatic face. In most cases, resulting in-situ dates are approximately 30% older than corresponding alpha-ejection corrected whole-grain dates, irrespective of the cooling rate and grain size. Whole-grain and in-situ dates are similar solely

20  
25  
30

35 for gem-size samples or samples exhibiting negligible diffusional helium loss, and thus spent  
more at surface temperatures compared to their transit time through the partial retention zone.  
Reconstruction of cooling histories using in-situ (U-Th-Sm)/He data can be achieved through  
single measurements in several grains with varying grain size and/or effective uranium  
40 grain rim. In addition, statistical analysis of a large compilation of measured radionuclide  
variations in apatite and zircon grains reveals that radionuclide zoning strongly impacts  
whole-grain analyses, but can be directly measured with the in-situ method. Overall, our  
results suggest that in-situ measurements for (U-Th-Sm)/He date determination offer a means  
to extract meaningful cooling signals from samples with poor reproducibility from traditional  
45 whole-grain techniques.

## 1.0 Introduction

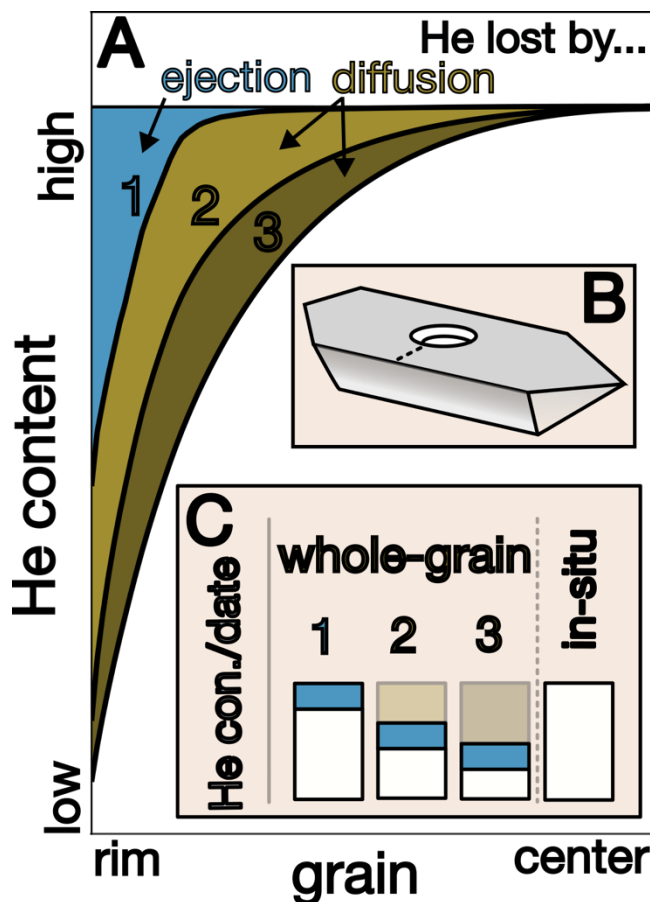
50 Alpha decay of radioisotopes and related ingrowth of  $^4\text{He}$  in crystal grains is the basis of the  
widely applicable (U-Th-Sm)/He method (e.g. Lippolt et al., 1994, Wolf et al., 1996, Farley,  
2002). A wide variety of minerals incorporate trace amounts of naturally occurring alpha-  
emitting isotopes such as U, Th, and Sm. Among those minerals, apatite and zircon have  
55 some favourable properties, making them a common choice for a wide range of applications  
to problems in tectonics and surface processes (e.g., Farley, 2000, 2002; Gallagher et al.,  
1998; Reiners and Ehlers, 2005; Malusà and Fitzgerald, 2019). Most importantly, apatite and  
zircon are abundant in many rock types, have a well-defined He diffusion behaviour (e.g.,  
Farley, 2000; Reiners, 2005; Hourigan et al., 2005; Flowers et al., 2009; Guenther et al.,  
60 2013), and are sensitive to upper crustal temperatures (e.g., Ehlers, 2005; Reiners and  
Brandon, 2006). Most applications of apatite and zircon (U-Th-Sm)/He thermochronometry  
make use of this and invert (U-Th-Sm)/He data to retrieve cooling histories of exhumed rocks  
(e.g. Wolf et al., 1996). The majority of (U-Th-Sm)/He thermochronometry studies use  
multiple whole-grain measurements from a single sample, often in combination with other  
65 thermochronometric data (e.g. Flowers 2009; Guenther et al., 2017; Falkowski et al., 2023).  
This is possible because He diffusion in apatite and zircon is controlled by grain size and  
accumulated radiation damage, both of which vary from grain to grain and thus lead to  
sample- and thermal history-specific relationships between these parameters. An alternative

method to reveal the near-surface thermal history of rocks is the  $^4\text{He}/^3\text{He}$  method (Shuster and Farley, 2004), which indirectly measures the He profile by stepwise degassing of He from proton-irradiated apatite grains.

Irrespective of the method applied, deriving accurate cooling histories is often difficult because of biases introduced by (i) fluid inclusion or inclusion of radionuclide-rich mineral phases (e.g., Farley, 2002; Ehlers and Farley, 2003; Vermeesch et al., 2007; Danišik et al., 2017), (ii) implantation of He from radionuclide-rich phases from outside the grain (Spiegel et al., 2009), and (iii) radionuclide zonation and related variability of diffusion caused by radiation damage (e.g., Hourigan et al., 2005; Fox et al., 2014, Anderson et al., 2017). Careful selection of euhedral grains free of visible inclusion can prevent large biases caused by the first process. In the case of detrital studies where understanding the date distribution is the objective, excluding grains can introduce bias in the resulting date distributions. The in-situ (U-Th-Sm)/He method theoretically provides less biased results since unsuitable parts of grains can be excluded from analyses (e.g., Tripathy-Lang et al., 2013). Radionuclide zoning and the implantation of He are usually not accounted for in common (U-Th-Sm)/He protocols. Implanted radiation damage in apatite and zircon and zonation, especially in zircon, increase the variance in whole-grain (U-Th-Sm)/He dates and are likely the main causes for overdispersed dates (e.g. Flowers et al., 2009; Horne et al., 2016, 2019).

In this regard, the introduction of the in-situ (U-Th-Sm)/He method by Boyce et al. (2006), has the potential to resolve some of the issues related to whole-grain analyses. However, in-situ dating has not become a routine alternative to whole-grain measurements, despite several studies demonstrating the reliability of dating large and/or rapidly cooled monazite, zircon, and apatite age standards (e.g. Boyce et al., 2006; Tripathy-Lang et al., 2013; Evans et al., 2015). One potential issue is the complex geometric relation between radionuclides and produced He, originating from long-alpha stopping distances (up to several tens of microns) and separation of daughter product from sourced parental radionuclide (e.g., Farley et al., 1996). Another potential issue is that more common small grains with less rapid cooling suffer from partial He loss by diffusion and thus should result in older whole-grain dates compared to in-situ (U-Th-Sm)/He dates (e.g. Tripathy-Lang et al., 2013). He loss by diffusion mainly occurs in the outer part of a grain (Fig. 1A). An in-situ He measurement in the center of a grain (Fig. 1B), results in a date that is similar to a whole-grain date only for cooling scenario 1 that involves rapid cooling to the surface, followed by a prolonged stay at the surface (Fig. 1C). In cooling scenarios 2 and 3 that involves a longer time at temperatures

where He diffusion is occurring, in-situ dates are older compared to whole-grain dates (Fig. 1C).



105 Fig. 1: Whole-grain vs. in-situ (U-Th-Sm)/He dates for end-member He profiles. A) Modelled He profiles for three cooling histories assuming uniform radionuclide distributions: 1) Rapid cooling to surface temperature, followed by a prolonged stay at the surface. 2) Constant slow cooling. 3) Prolonged stay in the partial retention zone, followed by rapid cooling to the surface. The blue area is the He content lost by alpha ejection, whereas He lost by diffusion is shown in brown. B) Cylindrical grain with ablation pit and location of He profiles in A. C) Corresponding He concentrations and resulting whole-grain and in-situ (U-Th-Sm)/He dates for the cooling histories in 1, 2 and 3. Note that ejected He (blue bar) is added to the measured He (white bar) in the whole-grain approach based on grain geometry (Ft-correction). The corresponding in-situ dates calculated for a central pit are identical  
110 irrespective of cooling histories and are similar to the whole-grain date only for the rapid cooling scenario (1). In all other cases, He is lost by diffusion, especially in the outer part of grains and in-situ (U-Th-Sm)/He dates are older compared to a whole-grain (U-Th-Sm)/He dates.  
115

120 In this study, we explore the theoretical measurement procedures required to interpret in-situ  
(U-Th-Sm)/He dates to retrieve cooling histories from multiple measurements in several  
grains or from a single grain. To do this, we simulate the He concentration across grains as a  
function of grain size/shape, radionuclide zoning and cooling history. These predicted He-  
distributions across grains are used to investigate the theoretical relationship between the size  
125 and position of in-situ laser ablation spots and the corresponding in-situ (U-Th-Sm)/He dates.  
The in-situ modelled dates are then compared to modelled whole-grain dates to identify the  
usability and limitations of each technique. In addition, the effect of radionuclide zoning in  
apatite and zircon on whole-grain dates is studied based on a large LA-ICP-MS dataset. We  
find that theoretically single in-situ (U-Th-Sm)/He measurements from different grains from  
130 the same sample, or multiple measurements within a single grain can be successfully inverted  
to retrieve consistently complex cooling histories similar to whole-grain analyses.

## 2.0 Methods

135

### 2.1 Modelling approach for He production, ejection and diffusion

The in-situ (U-Th-Sm)/He method is based on the extraction of He, U, Th and Sm from a  
small fraction of the grain using a laser ablation system (e.g. Boyce et al., 2006; Tripathy-  
140 Lang et al., 2013; Evans et al., 2015; Anderson et al., 2017; Pickering et al., 2020). Ablation  
pits can have a radius of a few tens of  $\mu\text{m}$  and depths of a few  $\mu\text{m}$  (e.g., from an excimer  
laser). Importantly, the ratio of He to U, Th and Sm (and therefore the date) varies with the  
size and position of the laser ablation measurements and likely differs from corresponding  
whole-grain (U-Th-Sm)/He dates. This, however, does not mean that dates are wrong or not  
145 interpretable; instead, they require a refinement of the interpretation steps commonly applied  
to (U-Th-Sm)/He data.

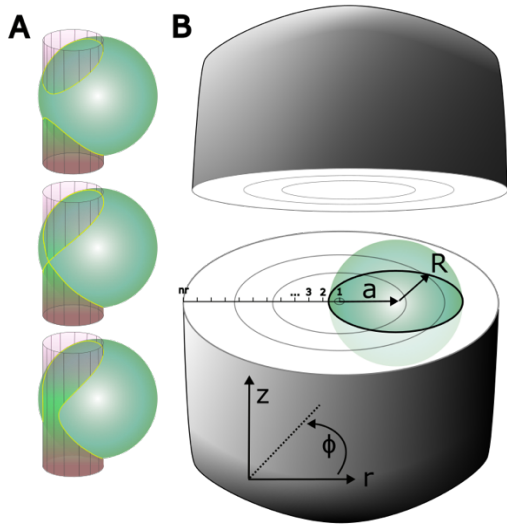
Whole-grain (U-Th-Sm)/He analyses often use a sphere-equivalent radius and assume  
spherical isotropic diffusion to estimate whole-grain He production, ejection, and diffusion in  
apatite/zircon crystals (e.g. Farley et al., 1996; Meesters and Dunai, 2002). More effort is  
150 required to match grain geometry for the in-situ (U-Th-Sm)/He method since long-alpha  
stopping distances (up to several tens of  $\mu\text{m}$ ) result in a complex geometric relation between  
the location of radionuclides (U, Th and Sm) and the resulting position of produced He. Most  
apatite grains have a prismatic geometry, with typical length/radius ratios of 4-8 (Farley,

2000). Loss of He by ejection and diffusion mostly occurs perpendicular to the  
155 crystallographic c-axis in prismatic grains such as apatite and zircon, and thus the He profile  
should be approximated for most grains with a finite cylinder model (Meesters and Dunai,  
2002). Farley et al. (2011) provide a method to transform measured element concentrations  
from cylindrical grains into an equivalent spherical-geometry, thereby providing input in the  
commonly used modelling software HeFTy (e.g. Danišik et al., 2017). Complementary to this  
160 approach, here we used the available spherical model implemented in HeFTy (Ketcham,  
2005) and modified it to handle an infinite cylinder geometry. The latter should be a good  
approximation for in-situ measurements outside the tips/caps of the analyzed grains where  
alpha-ejection effects become more significant. The advantage of an infinite cylinder model  
(compared to a finite cylinder model) is that it can be solved in 1D and thus runs as fast as the  
165 spherical model, a prerequisite for applying efficient inverse thermal history modelling. We  
adjusted the available He production, ejection, and diffusion models implemented in HeFTy  
(Ketcham, 2005; Flowers et al., 2009; Guenther et al., 2013) to handle an infinite cylinder  
geometry. More specifically, we implemented our changes to the existing C++ code (kindly  
provided by R. Ketcham) that simulates He diffusion following the RDAAM (apatite,  
170 Flowers et al., 2009) and ZRDAAM (zircon, Guenther et al., 2013) diffusion and annealing  
models. The modified version of RDAAM and ZRDAAM code is available from the Zenodo  
repository (<https://doi.org/10.5281/zenodo.13898183>).

## 175 2.2 Geometric considerations for He production, ejection and diffusion

The amount of He produced vs. ejected and diffused out of the grain depends on the  
concentration and distribution of parent isotopes and the grain morphology. These effects  
differ in spherical and cylindrical grains, especially if grains are zoned. Spherical zonation  
180 has been implemented in diffusion models for spheres (e.g., in HeFTy), which we also  
explore here for an infinite cylinder geometry. For simplicity, we assume that radionuclide  
zoning is symmetric around the c-axis for cylindrical grains (Fig. 2). Note that this might not  
always be applicable, especially to zircon grains, which apart from concentric parent nuclide  
distributions also reveal patchy/chaotic patterns (e.g. Chew et al. 2017; Danišik et al. 2017;  
185 Fox et al. 2017). It is therefore recommended that such a simplified approach is only applied  
to grains satisfying concentric parent nuclide distributions. Radionuclide zoning and grain  
size (especially the distance to the grain rim) control the amount of He along the radius ( $r$ -

axis), without diffusion. The He distribution along the r-axis is derived by calculating the intersecting lines of all alpha-ejection spheres (ranging from ~6 to ~40 μm) and internal cylinders with a radius defined by the grain size and grid spacing. The intersection line can consist of two closed curves, a continuous line, or, if the cylinder and the sphere are tangential to each other at one point, the line forms an ‘eight’ geometry, also known as Viviani’s curve (Fig. 2A).



195 Fig. 2: Geometric relationship between alpha-ejection spheres (green) and intersecting inner grain coaxial cylindrical surface representing variable radionuclide concentrations in a cylindrical grain (light grey lines). A) The length of a line defining the intersection between the cylinder and a sphere depends on the size of each object and its position. B) Assumed cylindrical grain with radionuclide zoning parallel to the z-axis is intersected by an alpha-ejection sphere with radius R and distance from the centre of a. The modelled He profile is discretized from the centre of the grain to the rim with nodes from  $i=1 \dots nr$ .

The procedure for calculating the amount of He in an infinite cylinder without diffusion along the r-axis is:

205

1. The grain is discretized by a number of cylinders  $(r, \Phi, z)$ , and the circular shape of the cylinders in  $r, \Phi$ -plane is transformed in  $x, y$ -coordinates:

$$x_{r,\phi} = r \cos(\Phi) \tag{1}$$

210  $y_{r,\phi} = r \sin(\Phi) \tag{2}$

2. The  $z$ -coordinates of the intersection line between the cylinder and the alpha-ejection sphere (the yellow line in Fig. 2A) are calculated with:

$$z_{r,\phi,R,a} = R^2 - (x_{r,\phi} - a)^2 - y_{r,\phi}^2 \quad (3)$$

where  $R$  is the radius of the alpha-ejection sphere, and  $a$  is the distance between the centre of the cylinder and the alpha-ejection sphere, and  $\Phi$  and  $r$  are the same as in Fig. 2B.

3. The length of the intersection line is calculated with the Pythagorean theorem:

$$l_{r,R,a} = 2 \sum_{i=1}^{n\Phi-1} \sqrt{\left(x_{r,R,a}(\Phi_i) - x_{r,R,a}(\Phi_{i+1})\right)^2 + \left(y_{r,R,a}(\Phi_i) - y_{r,R,a}(\Phi_{i+1})\right)^2 + \left(z_{r,R,a}(\Phi_i) - z_{r,R,a}(\Phi_{i+1})\right)^2} \quad (4)$$

where  $\Phi$  has been discretized from 0 to  $2\pi$  into  $i=1 \dots n\Phi$ .

4. Next, the length is normalized to unity:

$$\check{l}_{r,R,a} = \frac{l_{r,R,a}}{\sum_{i=1}^{na} l_{r,R}(a_i)} \quad (5)$$

230

where  $a$  has been discretized from  $r=0$  to the rim into  $i=1 \dots na$ .

5. Finally, we derived the radionuclide-specific concentration ( $C_{I,a}$ ) for isotopes ( $I$ ) and points ( $a$ ) along the  $r$ -axis with:

235

$$C_{I,a} = \sum_{j=1}^{nR} F_{I,j} \sum_{i=1}^{nr} \check{l}_{r,a}(R_j) C(r_i) \quad (6)$$

where  $F_{I,j}$  is the fractional contribution of an isotope-specific stopping distance and  $C$  is the radionuclide concentration depending on  $r$ .

240

The resulting He distribution is very similar to a spherical grain but with an overall higher concentration (for similar radii) since we assume an infinite length of the cylinder (Fig. 3A,B). Consequently whole-grain and in-situ (U-Th-Sm)/He dates of a cylindrical grain are



245 significantly older (in-situ: 19-27%, whole-grain: 11-12%) compared to a spherical grain with similar radii (Fig. 3C,D). Incorporating He diffusion and alpha-stopping distances leads to smooth (uniform radionuclides) or complex (zoned grains) He profiles (Fig. 3,6).

### 250 2.3 Calculation of He diffusion

250

Assuming a spherical grain geometry provides a good estimate of whole-grain He diffusion in apatite crystals (e.g., Farley et al., 1996; Meesters and Dunai, 2002). However, most apatite and zircon grains have a prismatic shape with hexagonal (apatite) and quadratic (zircon) cross-sections. Efficient modelling of He profiles requires a 1D solution of the diffusion equation and therefore a round cross-section, which can accurately predict He concentrations in apatite and zircon (cf. Eq. 19 and 20 and section 2.5). In the following, we solved the production and diffusion equation for an infinite cylinder (Farley, 2000). The 3D diffusion equation in a cylinder is:

$$260 \quad \frac{1}{r} \frac{\partial}{\partial r} \left( rK \frac{\partial v}{\partial r} \right) + \frac{1}{r^2} \frac{\partial}{\partial \phi} \left( K \frac{\partial v}{\partial \phi} \right) + \frac{\partial}{\partial z} \left( K \frac{\partial v}{\partial z} \right) + A_0 = \frac{\partial v}{\partial t} \quad (7)$$

where  $v$  is the He quantity,  $K$  is the diffusivity,  $t$  is time,  $A_0$  is the volumetric He production, and  $r$ ,  $z$  and  $\phi$  are the radial, vertical and azimuth positions (e.g., Fig. 2B). Assuming an infinite length of the cylinder and that He does not vary with  $z$  and  $\phi$ , the equation (Eq. 7) simplifies to:

265

$$\frac{1}{r} \frac{\partial}{\partial r} \left( rK \frac{\partial v}{\partial r} \right) + A_0 = \frac{\partial v}{\partial t} \quad (8)$$

Using the product rule, we get:

270

$$\frac{K}{r} \frac{\partial v}{\partial r} + K \frac{\partial^2 v}{\partial r^2} + A_0 = \frac{\partial v}{\partial t} \quad (9)$$

We solved Equation 9 with an implicit Euler finite difference method with the following assumptions: (i) grain symmetry (including geometry and radionuclide distribution) around

275 the  $z$ -axis, (ii) zero-flux Neumann boundary condition in the centre of the grain (Eq. 10), and  
 (iii) zero He concentration at the grain boundary (Eq. 11):

$$\frac{\partial v}{\partial r} = 0 \text{ for } r=0 \quad (10)$$

$$v = 0 \text{ for } r=r_{im} \quad (11)$$

280

Reformulating equation (Eq. 9 and 10) with the implicit Euler method yields:

$$\frac{v_i^{t+1}-v_i^t}{\Delta t} = \frac{K}{r} \frac{v_{i-1}^{t+1}-v_{i+1}^{t+1}}{\Delta r} + K \frac{v_{i-1}^{t+1}-2v_i^{t+1}+v_{i+1}^{t+1}}{\Delta r^2} + A_0 \quad \text{for } r>0 \text{ \& } r<r_{im} \quad (12)$$

$$\frac{v_i^{t+1}-v_i^t}{\Delta t} = K \frac{v_{i-1}^{t+1}-v_{i+1}^{t+1}}{\Delta r} + A_0 \quad \text{for } r=0 \quad (13)$$

285

Since  $i=-1$  is not defined, but similar to  $i=+1$ , it is common to instead use the second derivative and Eq. 13 changes to:

$$\frac{v_i^{t+1}-v_i^t}{\Delta t} = K \frac{2v_{i+1}^{t+1}-2v_i^{t+1}}{\Delta r^2} + A_0 \text{ for } i=0 \quad (14)$$

290

Solving Equation 14 requires a tridiagonal matrix whereby all unknowns ( $t+1$ ) are brought to the left-hand side:

$$(1 + 2D)v_i^{t+1} - 2Dv_{i+1}^{t+1} = v_i^t + A_0\Delta t \quad \text{for } i=0 \quad (15)$$

$$295 \left(-\frac{D\Delta r}{r} - D\right)v_{i-1}^{t+1} + (1 + 2D)v_i^{t+1} + \left(\frac{D\Delta r}{r} - D\right)v_{i+1}^{t+1} = v_i^t + A_0\Delta t \quad \text{for } r>0 \text{ \& } r<r_{im} \quad (16)$$

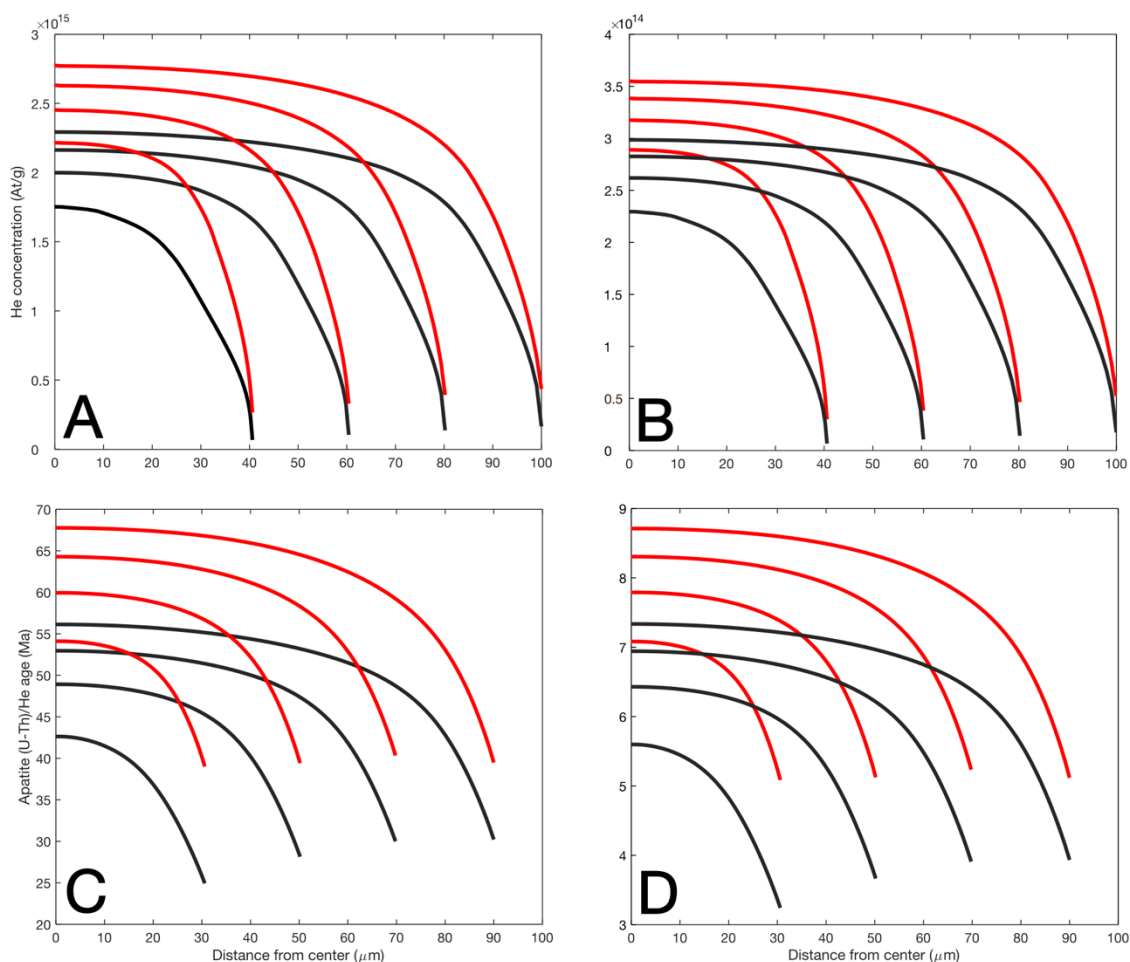
$$v_i^{t+1} = 0 \quad \text{for } r=r_{im} \quad (17)$$

where  $D$  is  $K\Delta t/\Delta r^2$ , and the corresponding tridiagonal matrix needed to solve for diffusion in an infinite cylinder is given by:

300

$$\begin{pmatrix} 1 + 2D & -2D & 0 & 0 & \dots & 0 \\ -\frac{D\Delta r}{r} - D & 1 + 2D & \frac{D\Delta r}{r} - D & 0 & \dots & 0 \\ 0 & -\frac{D\Delta r}{r} - D & 1 + 2D & \frac{D\Delta r}{r} - D & \dots & 0 \\ \vdots & \vdots & \vdots & \vdots & \ddots & \vdots \\ 0 & 0 & 0 & 0 & 0 & 1 \end{pmatrix} \begin{pmatrix} v_{i=0}^{t+1} \\ v_{i=1}^{t+1} \\ v_{i=2}^{t+1} \\ \vdots \\ v_{i=r+1}^{t+1} \end{pmatrix} = \begin{pmatrix} v_{i=0}^t + A_0\Delta t \\ v_{i=1}^t + A_0\Delta t \\ v_{i=2}^t + A_0\Delta t \\ \vdots \\ 0 \end{pmatrix} \quad (18)$$

305 The resulting He profiles for infinite cylinders have similar shapes as a sphere, but higher He  
 concentrations than a sphere with the same radius (Fig. 3A,B). The difference in  
 concentration between the infinite cylinder and sphere geometry (for constant cooling) is in  
 the range of 15-20% in the centre of the grain, comparable to previous observations  
 (Meesters and Dunai, 2002). Corresponding in-situ dates are 19-27% older in an infinite  
 cylinder compared to a sphere model with a similar grain radius, while whole-grain dates (not  
 310 shown) differ by 11-12%. The choice of geometry to model in-situ (U-Th-Sm)/He dates  
 matters even more than for the whole-grain method.



315 Fig. 3: Difference between He diffusion profiles and in-situ (U-Th-Sm)/He dates in a sphere  
 (black) and infinite cylinder (red) perpendicular to the c-axis with grain radii of 40, 60, 80  
 and 100 μm. All profiles are calculated for apatite grains applying the production, ejection  
 and diffusion with homogenous U, Th and Sm distributions (10 ppm), and constant cooling  
 rates of 1°C/Myr (A,C) and 10°C/Myr (B,D). In-situ (U-Th-Sm)/He dates of infinite cylinder

grains are 19-27% older compared to spheres with similar radii, whereas corresponding whole-grain (U-Th-Sm)/He dates differ by 11-12%.

320

A cylindrical model is a good approximation for the He profile in hexagonal apatite grains (Meesters and Dunai, 2002), but it is unclear what radius should be used to estimate the He profile. To determine the appropriate cylinder radius to approximate diffusion in a hexagonal grain, we calculated the 2D (cross-sectional) He distribution of an infinitely long symmetrical hexagonal grain with circumradius  $r_c$  between 30-50  $\mu\text{m}$  and corresponding infinite cylinders with variable radii. We calculated the difference between the mean He profile of the hexagonal and cylindrical grains and found that the circle-equivalent radius (CER) of a symmetrical hexagonal grain is simply the radius of a circle with a similar area:

325

$$330 \quad CER_{ap} = \sqrt{\frac{3\sqrt{3}r^2}{2\pi}} \approx 0.9094r \quad (19)$$

where  $r$  is the outer radius (touching all vertices) of a symmetrical hexagon. Equivalent to a zircon with a quadratic cross-section, we derived the following:

335

$$CER_{zr} = \sqrt{\frac{2r^2}{\pi}} \approx 0.5642r \quad (20)$$

where  $r$  is the outer radius of a quadrate.

340

#### 2.4 Implementation of alpha-stopping distances

During alpha decay, energy is released that leads to long alpha-stopping distances (e.g., Bragg and Kleeman, 1905). The common radiogenic isotopes  $^{238}\text{U}$ ,  $^{235}\text{U}$ ,  $^{232}\text{Th}$ , and  $^{147}\text{Sm}$  release alpha decay energies between 2233 keV ( $^{147}\text{Sm}$  to  $^{143}\text{Nd}$ ) to 8784 keV ( $^{212}\text{Po}$  to  $^{208}\text{Pb}$  as part of the decay chain of  $^{232}\text{Th}$ ). In total, the alpha decay of these radionuclides produces 216 different energies, each occurring with a different probability (Fig. 4). The relation between energy and stopping distance has been measured and calculated and is easily

345

accessible from the SRIM data collection (e.g., Farley et al., 1996; Ketcham et al., 2011).

350 Alpha particles produced from  $^{238}\text{U}$ ,  $^{235}\text{U}$ , and  $^{232}\text{Th}$  have stopping distances between  $\sim 11$  and  $\sim 40$   $\mu\text{m}$  in apatite (Fig. 4A-C), and those derived from  $^{147}\text{Sm}$  have a single stopping distance of  $\sim 6$   $\mu\text{m}$ . Integration of the stopping distance distribution yields the average stopping distances (Fig. 4A-C), commonly used to approximate He distribution profiles and  $F_T$  correction factors for whole-grain analyses (e.g., Ketcham et al., 2011). Note that the reported 355 values using the SRIM 2013 data show only very small differences from those of Ketcham et al. (2011), which is based on SRIM 2008.

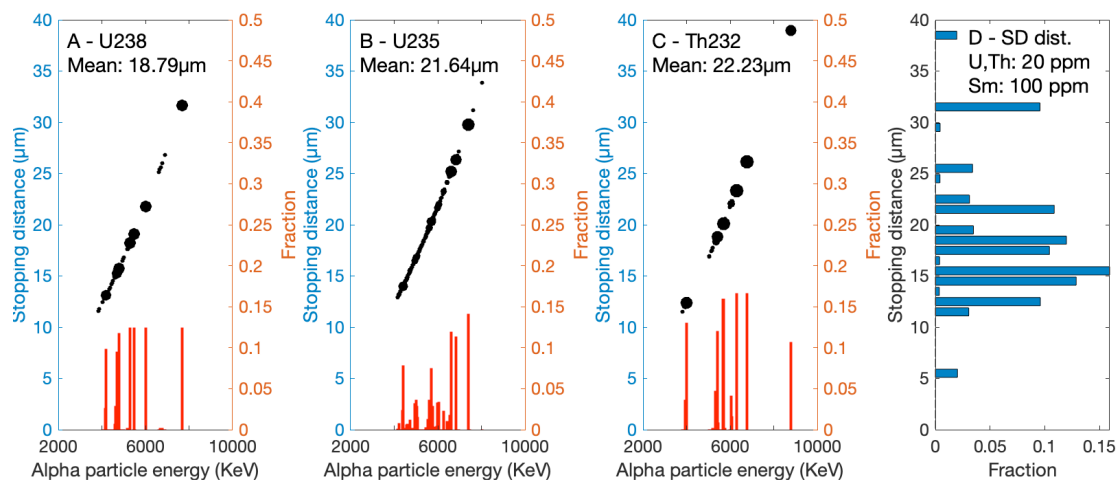


Fig. 4: Alpha particle energy spectra of  $^{238}\text{U}$  (A),  $^{235}\text{U}$  (B), and  $^{232}\text{Th}$  (C) and the

360 corresponding stopping distance spectra and mean stopping distances derived from SRIM2013 data assuming a fluorine apatite with a density of  $3.2 \text{ g/cm}^3$ . The stopping distance distribution (SD dist.) of a typical apatite with 20 ppm U and Th, and 100 ppm Sm is shown in (D).

365 Depending on the relative concentration of radionuclides, each mineral crystal will have a grain-specific alpha-stopping distance distribution (Fig. 4D). The majority of stopping distances in apatite are between 11 and 26  $\mu\text{m}$ , with additional peaks at 6  $\mu\text{m}$ , 32  $\mu\text{m}$ , and 39  $\mu\text{m}$  for a common apatite (Fig. 4D). Stopping distances in zircons are shorter and less variable, ranging from 9 to 32  $\mu\text{m}$ , while the majority are between 10 and 26  $\mu\text{m}$  long (Fig. 370 S1). Due to the long alpha-stopping distances, the in-situ measured He in an infinitely small area within the grain is produced from the surrounding  $\sim 6$  to 39  $\mu\text{m}$  and  $\sim 9$  to 32  $\mu\text{m}$  in apatite and zircon, respectively. Importantly, He originates from the surface of spheres with a radius corresponding to the stopping distance distribution (Fig. 2,5). This does not have large

consequences for grains with a homogenous radionuclide distribution, but He and radionuclide distributions do not follow a 1:1 relation in the case of radionuclide heterogeneity in grains (Fig. 5).

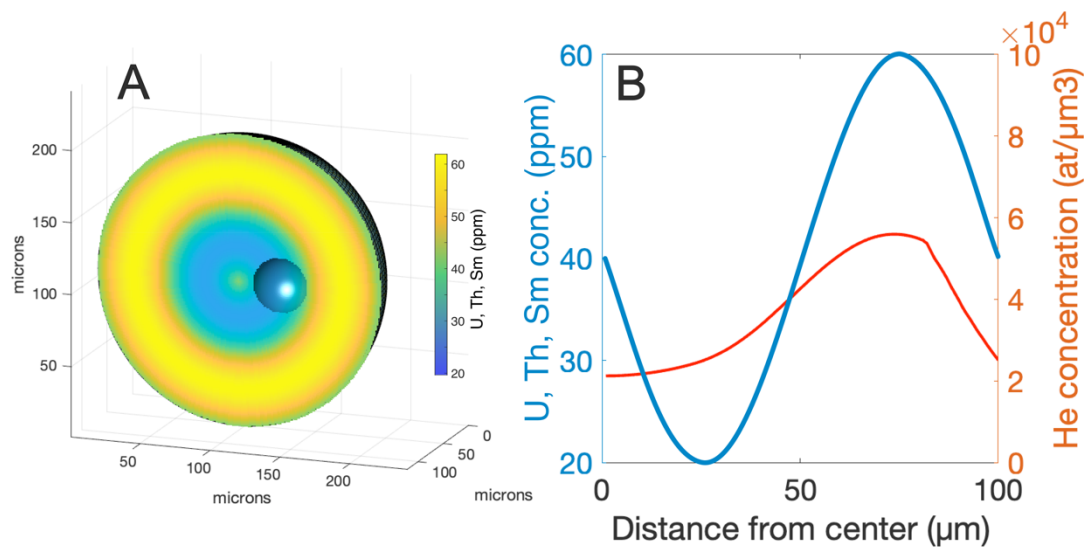
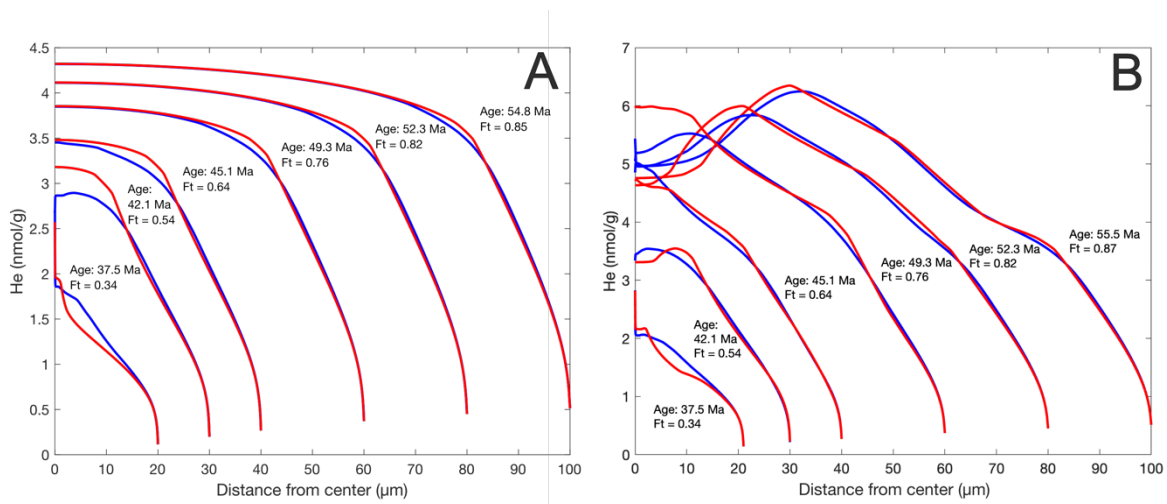


Fig. 5: Relationship between radionuclide zonation and resulting He profiles in a spherical apatite grain. A) Spherical grain with radial U, Th and Sm concentrations between 20 to 60 ppm, respectively. The small half-sphere corresponds to a stopping distance of 20  $\mu\text{m}$ . B) U, Th, Sm and resulting He concentrations from the core to the rim of the grain shown in A.

As a consequence, we adjusted the original RDAAM and ZRDAAM c++ implementation of HeFTy to (i) handle the full spectrum of stopping distances (instead of using an averaged value) of respective radionuclides and (ii) incorporate inner grain radionuclide variations. We tested our extended implementation against the original implementation for a theoretical spherical apatite grain (Fig. 6). The resulting whole-grain dates are indistinguishable from each other but the He profiles produced are smoother and, in some cases, show distinct differences (Fig. 6). Considering the full spectrum of stopping distances results in an overall lowering of the He concentration when approaching the grain rim for uniform radionuclide distributions (Fig. 6A). The incorporation of longer stopping distances (up to 39  $\mu\text{m}$ ) results in reduced He production at a distance between the longest stopping distance and the mean stopping distance from the grain rim. The opposite effect (higher He concentrations nearer to the grain rim) originates from stopping distances shorter than the mean stopping distance (Fig. 6A). Spherical grains with a grain radius smaller than the longest stopping distance (39  $\mu\text{m}$ ) but larger than the mean stopping distance ( $\sim 20$   $\mu\text{m}$ ) show lower He concentrations since the production in the grain core is zero when the grain radius is smaller than the stopping

distance (Fig. 6A). Variations in radionuclides, such as at the boundary between the grain and exterior require consideration of the full spectrum of stopping distances for the case of in-situ (U-Th-Sm)/He analyses close to the grain rim (within 39  $\mu\text{m}$  from the grain rim). Similarly, a mean stopping distance approach results in dissimilar He profiles in zoned grains with radionuclide variations compared to considering the full spectrum (Fig. 6B). To give an example, a two times higher radionuclide concentration between half and three-quarters of the radius (measured from the centre) results in the largest differences in the He concentration in the centre of the grain. The latter is usually the target of in-situ (U-Th-Sm)/He analyses. We suggest that any in-situ (U-Th-Sm)/He analyses require considering the full spectrum of significantly contributing alpha-stopping distances. Although not investigated here, the  $^4\text{He}/^3\text{He}$  method might also benefit from considering this to predict more accurate He profiles (e.g., Shuster and Farley, 2004).



410 Fig. 6: Apatite He profiles and (U-Th-Sm)/He dates for a cooling rate of  $1^\circ\text{C}/\text{Myr}$ , variable grain sizes, and mean (red, original implementation) or complete stopping distances (blue, our implementation). A) Uniform U, Th and Sm concentration of 10 ppm. B) Same as in A) but with two times higher radionuclides between the half radius and  $3/4$  radius.

415

### 2.5 Circle Equivalent Radius (CER)

Modelling (U-Th-Sm)/He data is usually accomplished using a transient 1D axial-symmetric parameterization, where different grain morphologies are approximated with a spherical geometry with similar volume-to-surface area ratios. With this approach, a solution is calculated in 1-D (as a function of radius), and then integrated over the volume of the

420

equivalent sphere. It has been shown that this approach is accurate for common grain morphologies within a few percent, whereas an infinite cylinder can have a deviation of up to 7% (e.g. Meesters and Dunai, 2002). Here we explore if such an approach also applies to accurately estimating He profiles within grains. We modelled the He distribution of an infinite symmetrical hexagonal prism with an outer radius of 50  $\mu\text{m}$  (inner radius of 43.3  $\mu\text{m}$ ). We compared these results to those calculated with an infinite cylinder (Fig. 7). The CER for such a grain is  $\sim 45.5 \mu\text{m}$ . The mean He profile of the hexagonal prism after averaging all possible profiles from the centre of the grain to the edge are nearly identical to a cylinder with a radius of 45.5  $\mu\text{m}$ . This result is irrespective of the cooling history (Fig. 7). The He profile deviates substantially at the outermost 5-10  $\mu\text{m}$  between the long and short axis of a hexagon, which should be discarded if it is not exactly known where the short and long axes are relative to the location of measurement.

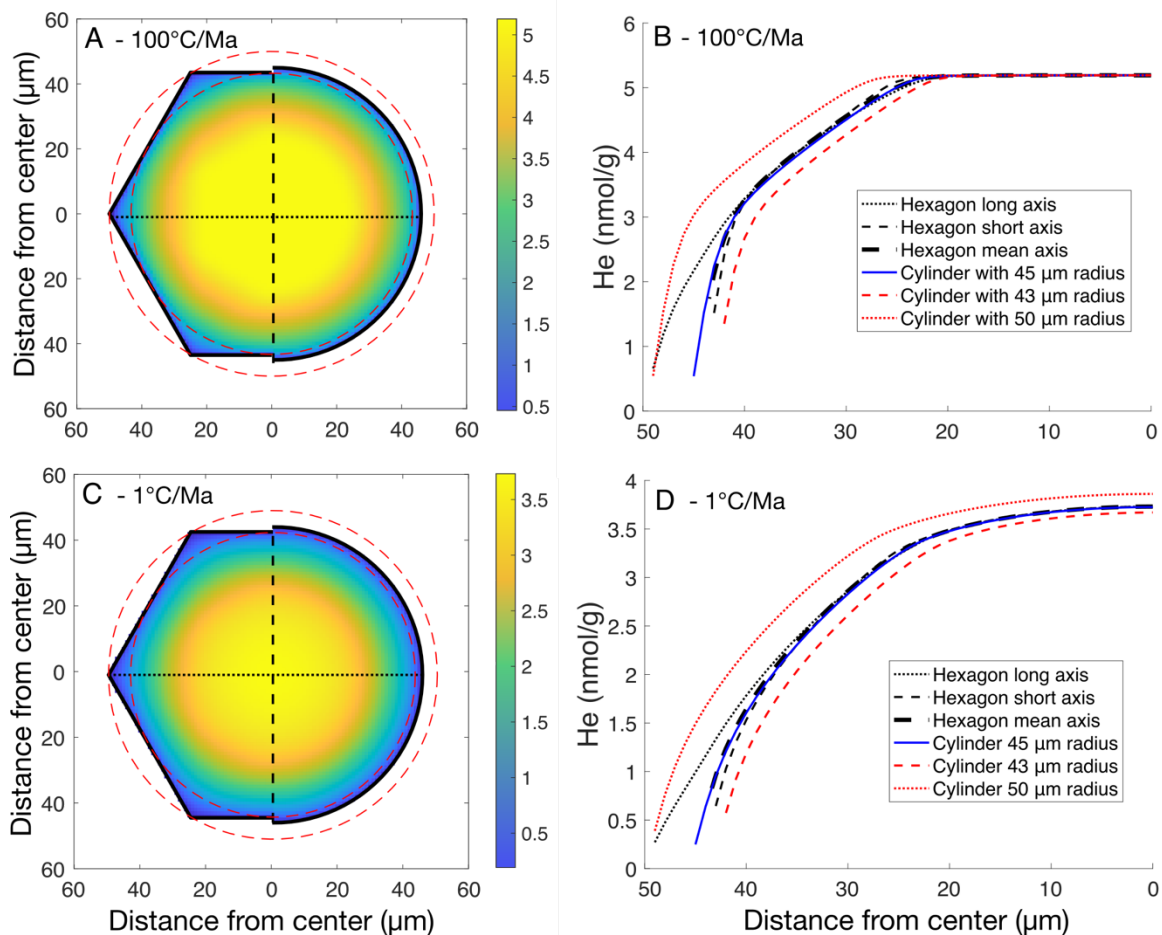


Fig. 7: He concentration in infinite hexagonal prism and cylinder. A) He concentration map modelled with RDAAM for a symmetrical hexagonal prism with an outer radius of 50  $\mu\text{m}$  and cylinder with a radius of 45.5  $\mu\text{m}$ , and 10 ppm U, Th and Sm concentrations, and rapid cooling (100°C/Myr) to surface temperature (10°C) at 60 Ma. B) Corresponding He profiles



440 for a hexagonal prism and infinite cylinder with different radii. C/D) Similar to A/B but for a  
constant cooling rate of 1°C/Myr.

## 2.6 Analytical uncertainty

445

In-situ (U-Th-Sm)/He dating relies on measuring pits that are only a few tens of microns in size, leading to increased analytical uncertainty, particularly in He measurements, compared to conventional whole-grain analyses. A typical cylindrical grain used in whole-grain measurements, with a diameter of 100  $\mu\text{m}$  and a length of 200  $\mu\text{m}$ , has a volume  
450 approximately 1000 times greater than a standard in-situ pit with a diameter of 30  $\mu\text{m}$  and 5  $\mu\text{m}$  depth. Consequently, in-situ analyses face significant analytical uncertainties, especially when applied to young samples or grains with low radionuclide concentrations. To report these limitations, we used the detection limit determined in our laboratory at the University of Tuebingen to model analytical uncertainties. The standard deviation of repeated line blanks  
455 ( $SD_{lb}$ ) gives a  ${}^4\text{He}$  of 0.000079 ncc or  $2.11 \times 10^6$  atoms. This allows for estimating the analytical uncertainty for modelled in-situ He content ( ${}^4\text{He}_m$ ) using the following equation:

$$u = \sqrt{\left(\frac{SD_{lb}}{{}^4\text{He}_m}\right)^2} \quad \text{Eq. 21}$$

This equation does not account for uncertainties related to the required measurement of radionuclides, which are generally small and around 2%.

460

## 3.0 Results

### 3.1 Whole-grain vs. in-situ (U-Th-Sm)/He dates

465

Whole-grain (U-Th-Sm)/He dates reflect the production, ejection, diffusion, and alpha-ejection correction for the complete grain. In contrast, in-situ (U-Th-Sm)/He dates, if measured in the centre of grains, are not affected by alpha ejection, less affected by diffusion, and do not require an alpha-ejection correction (e.g., Tripathy-Lang et al., 2013).

470

Theoretically, in-situ dates will, in most cases, differ from whole-grain dates from similar grains. The majority of in-situ (U-Th-Sm)/He studies applied so far used large crystals with

homogenous radionuclide distributions and/or rapidly cooled samples to enable comparison of the results to whole-grain measurements (e.g., Boyce et al., 2006; Horne et al., 2016).

475 Making this method applicable to small and/or slowly cooled grains requires understanding the relationship between the grain size, position and size of the ablation spots, radionuclide distribution, and resulting (U-Th-Sm)/He dates. To investigate these effects we considered several scenarios.

480 First, we modelled whole-grain and in-situ (U-Th-Sm)/He dates as a function of cooling rate (1, 10 and 40°C/Myr) for radionuclide concentrations of 10 ppm and a grain radius of 100  $\mu\text{m}$  (Fig. 8A-C). Modelled whole-grain dates are 49, 6.5 and 1.9 Ma for cooling rates of 1, 10 and 40°C/Myr, respectively. In-situ (U-Th-Sm)/He dates vary as a function of their measurement position in the grain. Assuming similar grain parameters and cooling rates, in-situ dates range between 48-65 Ma (1°C/Myr), 6.3-8.3 Ma (10°C/Myr) and 1.8-2.4 Ma (40°C/Myr) for a spot diameter of 20  $\mu\text{m}$  and grain radius of 100  $\mu\text{m}$  (Fig. 8A-C). Modelled in-situ dates measured 485 in the centre of grains are older than the whole-grain dates because the fraction of He lost by diffusion is smallest in the centre of grains and increases towards the grain boundary, as does He loss by alpha-ejection. Accordingly, in-situ dates become progressively younger towards the grain rim. A larger laser spot size averages over a larger area and may incorporate areas affected by He loss. A larger spot size, therefore, leads to younger dates, and a smaller spot size can be expected to produce less variation in dates, especially when analyzing smaller 490 grains. Modelled analytical uncertainties limit the applicability of the in-situ (U-Th-Sm)/He method for young grains (Fig. 8A,B). A spot diameter >50  $\mu\text{m}$  and therefore a grain with a diameter of ~100  $\mu\text{m}$  is required to reach uncertainties <100% for dates <10 Ma (Fig. 8A,B). Second, we simulated the effect of grain size on whole-grain and in-situ (U-Th-Sm)/He dates 495 for a cooling rate of 1°C/Myr, radionuclide concentrations of 10 ppm and grain radii of 100, 80, 50 and 40  $\mu\text{m}$  (Fig. 8C-F). Whole-grain dates decrease as a function of grain size from 49 to 39 Ma, while in-situ dates consistently result in older dates. In-situ measurements with similar spot diameter (e.g., 20  $\mu\text{m}$ ) sample larger fractions of areas affected by He loss and, therefore, in-situ dates become less sensitive to the measurement position in the grain for 500 smaller grains. In the most extreme case where the spot diameter corresponds to the grain radius the alpha-ejection corrected in-situ date would match the whole-grain date. In practice, the spot size also depends on the expected He concentration and must be determined based on the detection limit of He measurable with the instrumental setup and the maximum depth of laser pits that can be measured accurately.

505 Third, we studied the in-situ date dependency for cases in which grains have not been ground  
and polished to the exact centre of the grain (Fig. 8G,H). In-situ dates become progressively  
younger towards the grain rim compared to a measurement in the centre of the grain (Fig.  
8G,H). In a large grain (100  $\mu\text{m}$  radius, Fig. 8G), dates are similar within  $<40 \mu\text{m}$  from the  
central plane of the grain. In-situ dates in smaller grains are more sensitive to the position of  
510 the measurement relative to the grain rim (Fig. 8H).  
In summary, uniform cooling yields in-situ (U-Th-Sm)/He dates that are older than whole-  
grain dates, and dates strongly vary as a function of the measurement position relative to the  
grain rim. The results obtained here for apatite also apply to zircons, as has been revealed by  
modelling in-situ dates as a function of grain size, and position and size of the ablation spots  
515 with the ZRDAAM approach (Fig. S2). Measuring grain size and geometry, and the laser  
spot position relative to the grain rim is essential for correctly interpreting in-situ (U-Th-  
Sm)/He dates. The grain size and geometry, and location of laser pits on the grain surface can  
be easily determined with an optical microscope, whereas estimating the pit location in the  
vertical direction is difficult. A rough estimate ( $\pm 5 \mu\text{m}$ ) can be gained by focusing on the  
520 contact between grain and embedding media and measuring the distance to the exposed grain  
surface.

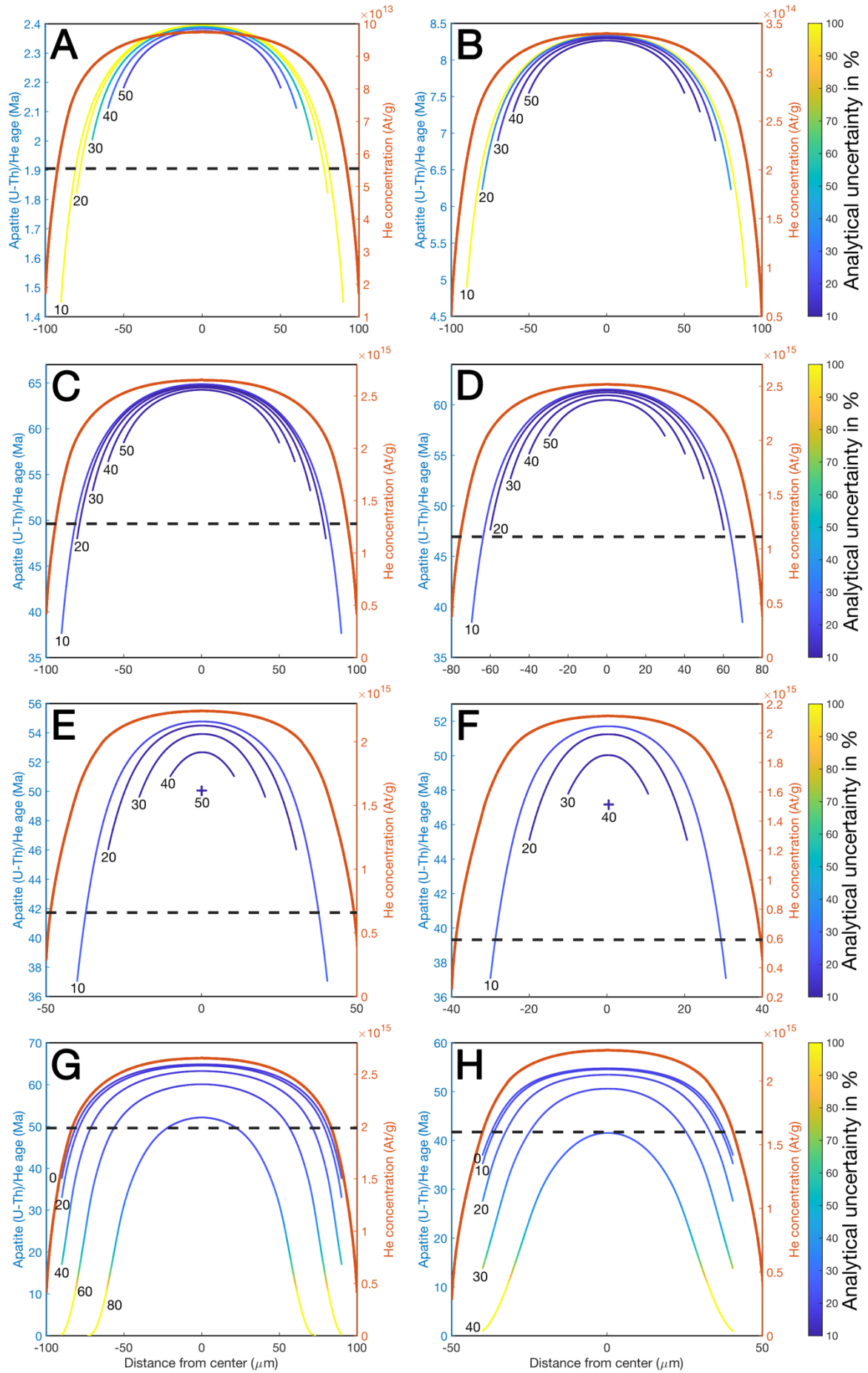


Fig. 8: Predicted in-situ apatite (U-Th-Sm)/He dates (blue to yellow lines) and He  
525 concentration profile (orange line) for an infinitely long, cylindrical-shaped apatite with  
homogenous radiogenic nuclide distribution (U, Th and Sm concentration of 10 ppm).  
Predicted dates are calculated by integrating the modelled He distribution over an entire  
ablation pit volume of variable diameters (black numbers on curves in A-H), which is  
continuously measured across the grain. In reality, discrete (rather than continuous) pits  
530 would be measured, and smooth curves such as those shown here would not be possible. In-  
situ date profiles are colour-coded according to expected analytical uncertainties calculated  
with an observed standard deviation of the  $^4\text{He}$  blank of 0.000079 ncc. A) Model results  
assuming a constant cooling rate of  $40^\circ\text{C}/\text{Myr}$  to a final temperature of  $10^\circ\text{C}$  and a grain  
radius of  $100\ \mu\text{m}$ . The corresponding whole-grain date for a sphere with a similar sphere-  
535 equivalent radius (radius\*1.5) corrected for alpha ejection is 1.9 Ma. Modelled in-situ dates  
with variable spot diameters (10, 20, 30, 40 and  $50\ \mu\text{m}$ ) range from 2.4 Ma in the centre of  
the grain to 1.45 Ma half the spot diameter away from the grain rim. B) Model results  
assuming constant cooling at  $10^\circ\text{C}/\text{Myr}$  to  $10^\circ\text{C}$  and a grain radius of  $100\ \mu\text{m}$ . The  
corresponding whole-grain date corrected for alpha ejection is 6.5 Ma. Modelled in-situ dates  
540 with variable spot diameters (10- $50\ \mu\text{m}$ ) range from 8.3 Ma in the centre of the grain to 4.8  
Ma half the spot diameter away from the grain rim. C) Model results assuming constant  
cooling at  $1^\circ\text{C}/\text{Myr}$  to  $10^\circ\text{C}$  and a grain radius of  $100\ \mu\text{m}$ . The corresponding whole-grain  
date corrected for alpha ejection is 64.9 Ma in the centre of the grain to 37.7 Ma half the spot  
diameter away from the grain rim. D,E,F) Same as C) but with a grain radius of 80, 50, and  
545  $40\ \mu\text{m}$ . The smaller grain radius results in younger whole-grain dates (47, 42, and 39 Ma,  
respectively) and a stronger relationship between in-situ dates and distance of measurement  
towards the grain rim. G) In-situ dates for a grain radius of  $100\ \mu\text{m}$  and spot diameter of  $10\ \mu\text{m}$ .  
Dates have been calculated for the central plane, dividing the cylinder into two  
symmetrical sides along the crystallographic c-axis (black number 0 -  $0\ \mu\text{m}$  in the r-direction  
550 of Fig. 2) and planes cutting the grain at 20, 40, 60, and  $80\ \mu\text{m}$  above/below the central plane.  
H) In-situ dates for a grain radius of  $50\ \mu\text{m}$  and spot diameter of  $10\ \mu\text{m}$ . Dates have been  
calculated for the central plane and at other r-planes 10, 20, 30,  $40\ \mu\text{m}$ .

555

### 3.2 Effects of radionuclide zoning

Without practical analytical measurement methods to quantify inner-grain variations in radionuclides, whole-grain analyses commonly use an a priori assumption of a uniform radionuclide distribution. The in-situ (U-Th-Sm)/He dating technique produces spatially  
560 resolved (albeit averaged over the ablation pit) measurements of U, Th, and Sm (e.g. Horne et al. 2016, Danišik et al., 2017). In-situ measurements can provide information about inner-grain radionuclide variations and potentially lead to a reduction in date variability when excluding grains with radionuclide variations or by taking into account heterogeneities in the radionuclides.

565 Ideally, however, the 2D-3D distribution of parent nuclide concentrations is mapped in grains, which is possible with a new generation of instruments, such as by mapping parent nuclide concentrations with laser-ablation inductively coupled plasma mass spectrometry (Chew et al. 2017), time-of-flight secondary ion mass spectrometry (North et al. 2022) or synchrotron X-ray fluorescence tomography (Sousa et al. 2024). Measured 3D radionuclide  
570 patterns can be incorporated in available implementations of 3D modelling of He production, ejection and diffusion (e.g. Gautheron et al. 2012). Although this procedure would be ideal, it is computationally and analytically expensive, and, therefore not routinely applied. Efficient thermal history modelling of (U-Th-Sm)/He data requires 1D modelling of He production, ejection and diffusion, which can be combined with time-efficient single-spot LA-ICP-MS  
575 measurements. This approach should be used to identify, and exclude, grains with complex radionuclide variations.

Here, we have analyzed several hundred LA-ICP-MS measurements done in our lab at the University of Tuebingen, Germany. The depth-resolved radionuclide measurements in apatite and zircon demonstrate that radionuclide zoning is common (supplement data SD1). Zoning  
580 is more common and pronounced in zircons; ~30% of all analyzed zircons have a core-to-rim ratio  $<0.5$  or  $>2$ , whereas this fraction is at ~10% for apatites (Fig. S4). Not accounting for radionuclide zoning results in erroneous Ft-correction factors and resulting whole-grain dates (e.g., Hourigan et al. 2005). Here, we use our updated production-ejection-diffusion model to calculate the relationship between whole-grain (U-Th-Sm)/He dates and radionuclide  
585 variations (Fig. 9).

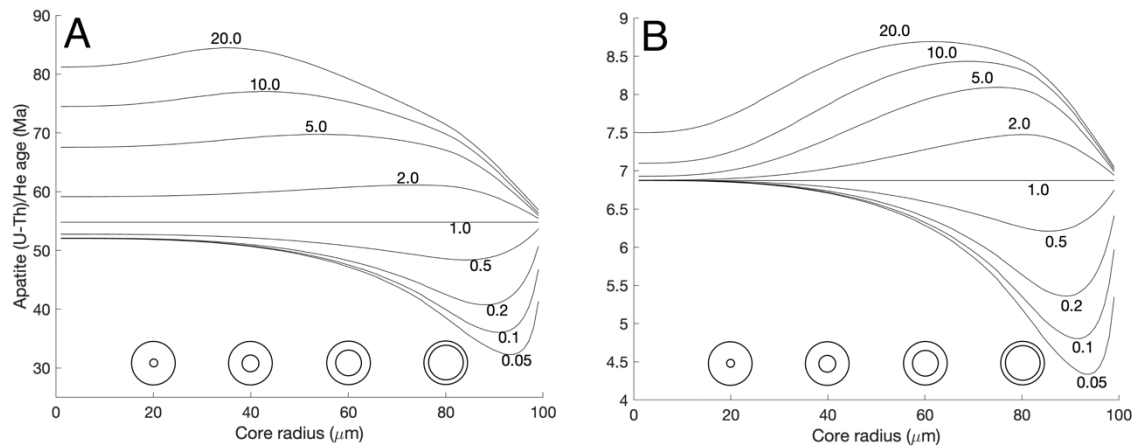


Fig. 9: Whole-grain apatite (U-Th-Sm)/He dates as a function of radionuclide variations (zoning). Isoline labels correspond to the core/rim ratio of radionuclides, assuming a single-step function in the concentration of U, Th, and Sm across the grain, where the x-axis specifies the location of the step in concentration. A) Dates for a cooling rate of 1°C/Myr and volume-averaged U, Th, and Sm concentration of 10 ppm. B) Dates for a cooling rate of 10°C/Myr and volume-averaged U, Th, and Sm concentration of 10 ppm.

590

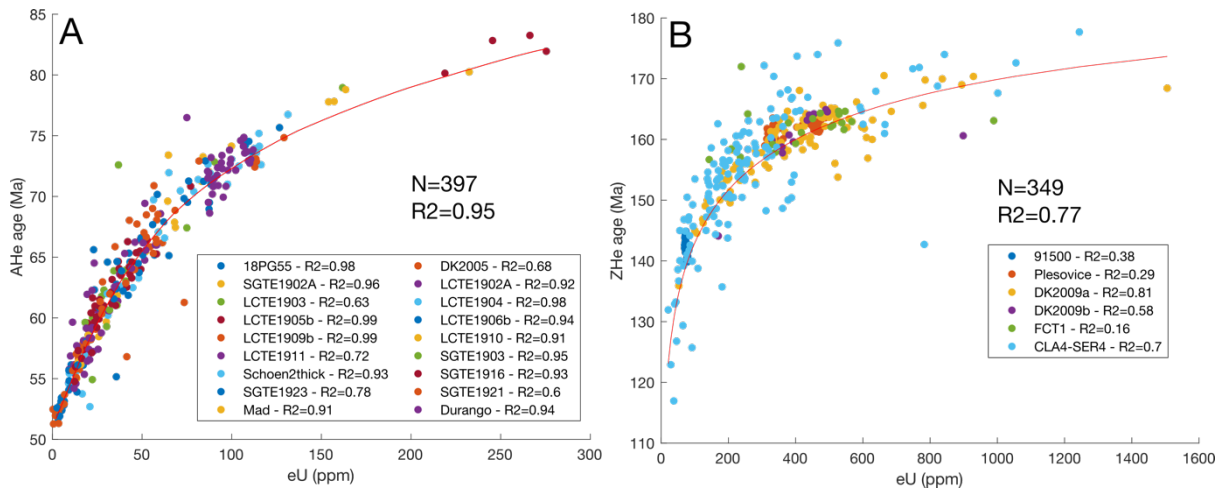
595 Commonly observed core-to-rim ratios between 0.5 and 2 lead to  $\pm 10\%$  date deviations (Fig. 9). Since observed radionuclide variations cannot be simplified with a single-step function (Fig. S3), we have scaled measured LA-ICP-MS derived depth variations to a grain radius of 100  $\mu\text{m}$  and calculated whole-grain apatite and zircon (U-Th-Sm)/He dates for a cooling rate of 1 °C/Myr (Fig. 10). Single-grain dates are mainly a function of the mean eU of individual grains, but depending on the amount of radionuclide zoning, dates deviate from the

600 corresponding date assuming homogenous radionuclide distribution (red line in Fig. 10). The correlation coefficient is 0.95 and 0.77 for all apatites and zircons, respectively, or, in other words, 5% and 23% of the variability in dates is the result of radionuclide zoning. Individual samples usually involve fewer grains with variations in dates caused by radionuclide zoning

605 ranging from 1 to 40% and 19 to 84% for analyzed apatites and zircons (Fig. 10), respectively. In samples with a low variation in eU and strong radionuclide zoning, the majority of variability is caused by zoning and there is no significant relation with eU. For example, in the analyzed Fish Canyon tuff zircons, 84% of the variations in dates is due to zoning (Fig. 10B). As mentioned earlier, additional age dispersion can come from crystal

610 fragmentation, radionuclide-rich inclusions, fluid inclusions and implantation of He from the exterior (e.g. Brown et al., 2013; Vermeesch et al., 2007; Spiegel et al., 2009; Danišik et al., 2017). It is, therefore, more likely to have overdispersed whole-grain (U-Th-Sm)/He dates,

and perfect relations between dates and eU will be the exception rather than the rule (Flowers et al., 2022).



615

Fig. 10: Simulated apatite (A) and zircon (B) (U-Th-Sm)/He dates for a constant cooling rate of 1°C/Myr, and measured grain-specific U, Th, and Sm variations (coloured dots).

Radionuclide variations were measured in age standards and random samples with a LA-ICP-MS system and scaled to a common grain size of 100 μm, assuming symmetric zoning

620

around the c-axis. This was used to model grain-specific whole-grain (U-Th-Sm)/He dates.

The red line represents the relation between dates and homogenous radionuclide distribution.

The correlation coefficient for the whole dataset and individual samples are shown. Note that the 1-R<sup>2</sup> is the fraction of spread caused by radionuclide zoning.

625

The observed radionuclide variations and resulting date dispersion in Figure 10 allow for estimating the minimum sample size required to reach a defined correlation coefficient between date and eU. We did this by randomly sampling 20,000 times 3, 4, 5 ...30 grains from our database and determined the relationship between the correlation coefficient and sample size. We found that a minimum of 10 apatite grains is needed to reach an R<sup>2</sup> of 0.8,

630

and an impractical 23 whole-grain ZHe dates are theoretically needed to reach a minimum R<sup>2</sup> of 0.5 (see supplement data SD3 for details).

In summary, whole-grain (U-Th-Sm)/He age variations with eU are often biased by radionuclide zonation. In in-situ (U-Th-Sm)/He studies, radionuclides are typically determined from a single pit, several tens of micrometer deep, drilled and analyzed using LA-

635

ICP-MS (e.g., Pickering et al., 2020). After applying a downhole fractionation correction to those data (Paton et al., 2010), depth-resolved radionuclide profiles in apatite and zircon grains enable the identification of zoned grains, which should be excluded from further analyses. Since this analytical step is mandatory for the in-situ (U-Th-Sm)/He method, single-



grain data should, in theory, lead to less dispersion in date vs. eU plots and likely also  
640 produce more reliable thermal history reconstructions. In contrast, including grains with  
identified radionuclide zoning is likely to produce inaccurate results, as helium is generated  
and measured from different volumes within the grain (e.g., Vermeesch et al., 2023).

### 3.3 Thermal history modelling of in-situ (U-Th-Sm)/He data

645

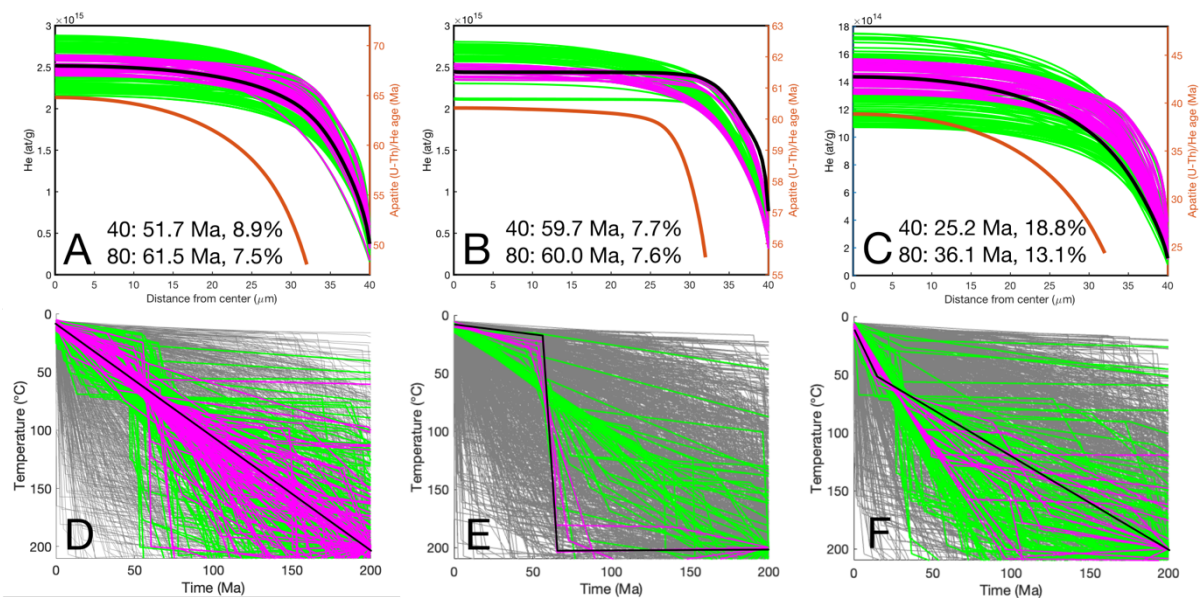
The relative distribution of He within an apatite or zircon grain is a function of the  
distribution of radionuclides, grain morphology, and the cooling history. A suite of whole-  
grain analyses can be used to reconstruct potential cooling histories under the precondition  
that analyzed grains have different grain sizes and/or eU (e.g., Ketcham, 2005; Flowers et al.,  
650 2009; Gautheron et al., 2009; Guenther et al., 2013). This approach, however, has the risk of  
including grains with internal variations in radionuclides, and is, therefore, often applied in  
combination with other thermochronometric systems (e.g., apatite fission track data). Similar  
to whole-grain analyses, radionuclide zonation can bias the interpretation of cooling histories  
derived from the apatite  $^4\text{He}/^3\text{He}$  method (Farley et al., 2010), which indirectly measures the  
655 He profile by a stepwise degassing of He from proton-irradiated apatite grains.

Thermal history modelling with in-situ (U-Th-Sm)/He data could be done by (i) measuring  
multiple grains that vary in size and/or eU similar to the whole-grain approach, or (ii)  
reconstructing the He profile with multiple measurements in a single grain comparable to the  
 $^4\text{He}/^3\text{He}$  method (e.g. Danišik et al., 2017). Both approaches are applied in the following to  
660 reconstruct common cooling paths from synthetic datasets. A robust methodology requires  
knowing or estimating (i) the grain geometry, (ii) the position of the in-situ measurements  
within the grain, (iii) the radionuclide distribution within the grain, and (IV) building an  
appropriate model to account for the previous factors.

In theory, complex grain morphologies could be used for such an approach, but this would  
665 require implementing grain-specific 3D models. Thermal history modelling with 3D models  
is time-consuming and, therefore, not practical for routine analysis. Similar to whole-grain  
analyses, it is therefore recommended to make in-situ measurements of grains with simple  
geometries characterized by straight and/or 2D-3D constant curvatures such as spherical,  
elliptical, and cylindrical shapes. Preferably, the in-situ measurement can be approximated  
670 with a 1D modelling approach similar to whole-grain and  $^4\text{He}/^3\text{He}$  analyses, where the  
sphere-equivalent radius has been shown to be a good approximation (e.g. Meesters and

Dunai, 2002; Farley et al., 2010). Unlike whole-grain and  $^4\text{He}/^3\text{He}$  analyses, the in-situ method requires modelling the He concentration within the ablated pit volume.

We conducted three different measurement approaches to evaluate the utility of in-situ dating techniques for thermal history reconstruction. First, a set of two cylindrical spots with 30  $\mu\text{m}$  diameter and 5  $\mu\text{m}$  depth in the centre of cylindrical-shaped grains with radii of 80 and 40  $\mu\text{m}$  and similar eU were forward-modelled with three different cooling histories: (1) a constant cooling rate of  $1^\circ\text{C}/\text{Myr}$ , (2) rapid cooling of  $100^\circ\text{C}/\text{Myr}$  at 60 Ma to surface temperature followed by no cooling, and (3) a step-increase in cooling rate from an initial  $1^\circ\text{C}/\text{Myr}$  until 10 Ma to  $50^\circ\text{C}$ , followed by  $4^\circ\text{C}/\text{Myr}$  cooling to surface temperature. Analytical uncertainties of theoretical He measurements were calculated with Eq. 21 and lab-specific blank level ( $2.11 \times 10^6$  atoms), resulting in uncertainties of  $\sim 8\%$  for cooling histories (1) and (2) and  $\sim 15\%$  for cooling history (3). Several thousand forward models were conducted, and the goodness-of-fit (GOF) of predicted cooling paths was determined. We used the same definition of the GOF and colour scheme as used in HeFTy (Ketcham, 2005). Good and acceptable model paths retrieve the input He profile and cooling paths especially in the center of grains, while modelled He concentrations deviate in the outer 20  $\mu\text{m}$  for some/most cooling paths (Fig. 11).



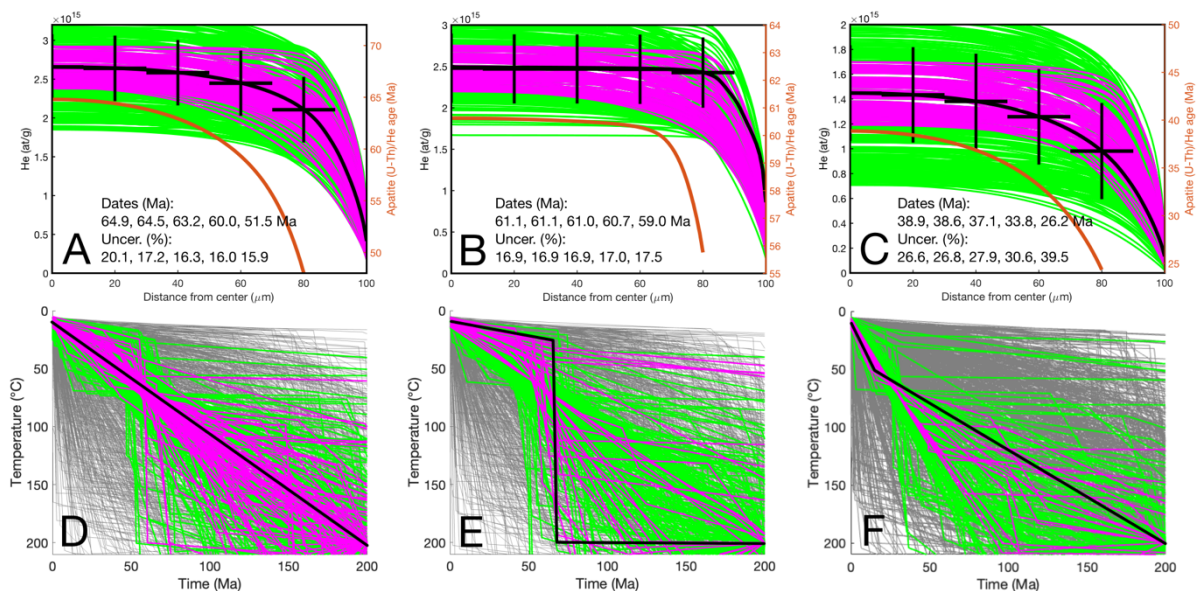
690 Fig. 11: Modelling of cooling histories for three synthetic datasets with two laser-ablation spot measurements in apatite grains with a pit diameter of 30  $\mu\text{m}$  (5  $\mu\text{m}$  depth), a grain radius of 80 and 40  $\mu\text{m}$  and U, Th, and Sm concentrations of 10 ppm. Upper panels (A,B,C) show the synthetic (black line) and modelled (green, magenta) He profiles, while the brown line represents the in-situ (U-Th-Sm)/He dates for the 40  $\mu\text{m}$  grain. The lower panels (D,E,F)

695 show the input (black) and modelled (gray, green, magenta) cooling paths. Predicted cooling histories with acceptable paths are green (GOF>0.05), good paths are magenta (GOF>0.5), and paths with a GOF<0.05 are grey. A,D) Data was calculated with a constant cooling rate of 1°C/Myr. B) Input data were modelled with rapid cooling at 60 Ma to surface temperature. C) Initial slow cooling with 1°C/Myr to 50°C at 10 Ma is followed by faster cooling to the surface with 4°C/Myr.

700

Second, a set of synthetically generated He measurements were taken along a profile in a single grain. We use a cylindrical grain with a radius of 100 μm and the same thermal histories as in the previous experiment. We sampled the He profile with an assumed cylindrical spot with a diameter of 20 μm and depth of 5 μm at five locations from the centre of the grain to the rim. The resulting He profiles and synthetic He measurements with uncertainties are shown in Fig. 12A-C. Analytical uncertainties of theoretical He measurements were calculated with Eq. 21 and lab-specific blank level ( $2.11 \times 10^6$  atoms), resulting in uncertainties of 16-20 % for cooling history (1) and (2) and ~26-40% for cooling history (3). Most acceptable cooling histories overlap or are close to the input parameters, suggesting that in-situ (U-Th-Sm)/He measurements within a single grain can be used to get information on its cooling history (Fig. 12D-F).

710



715 Fig. 12: Cooling histories predicted from in-situ (U-Th-Sm)/He measurements sampled along the He profile of a synthetic cylindrical apatite grain with a radius of 100 μm, and U, Th, and Sm concentrations of 10 ppm. Five 20 μm diameter (5 μm depth) ablation pits across the grain (horizontal black lines) are used as synthetic input data. Upper panels (A,B,C) do show synthetic (black line) and modelled (green, magenta) He profiles, while the brown line

represents the in-situ (U-Th-Sm)/He dates. Resulting in-situ (U-Th-Sm)/He dates and He  
720 uncertainties are also given from the center (left) to the rim (right). The lower panels (D,E,F)  
show the input (black) and modelled (gray, green, magenta) cooling paths. Predicted cooling  
histories with acceptable paths are green (GOF>0.05), good paths are magenta (GOF>0.5),  
and paths with a GOF<0.05 are grey. Data modelled with a constant 1°C/Myr cooling rate  
(A,D), a rapid cooling event at 60 Ma to surface temperature (B,E), and slow cooling with  
725 1°C/Myr to 50°C followed by faster cooling to the surface with 4°C/Myr from 10 Ma (C,F).

Although we would not recommend interpreting grains with internal radionuclide variations,  
here we investigate the consequences for in-situ and whole-grain thermal history modelling.  
We assume a scenario in which the outer 10 µm of grains is enriched in radionuclides (U, Th,  
730 Sm: 50 ppm) compared to the grain interior (U, Th, Sm: 10 ppm). This is a nasty scenario,  
resulting in largely underestimated whole-grain (U-Th-Sm)/He dates if not corrected for (Fig.  
9). Analogous to the previous thermal history modelling, a fast cooling from high  
temperature to surface temperature at 60 Ma was used to produce theoretical (U-Th-Sm)/He  
data for cylindrical grains with 100, 80 and 40 µm radii.

735 The general cooling trend can be retrieved in case the radionuclide distribution is precisely  
known and the He profile is sampled with several measurements in a single grain (Fig.  
13A,B) or multiple grains with variable sizes are analysed (Fig. 13G-J). We also tested the  
inversion performance assuming a homogenous radionuclide concentration of 10 ppm,  
measured for instance with a LA-ICP-MS pit in the centre of the grain (not reaching the grain  
740 rim). In addition, a homogenous radionuclide concentration of 17.6, 19.4 and 27.5 ppm for  
grains with 40, 80 and 100 µm radii was used as input, representing the grain averaged  
concentration, as measured through whole-grain analyses. As expected, observed inner-grain  
He variations, with increased concentrations toward the grain rim, are impossible to model  
with a constant radionuclide concentration (Fig. 13C-K). The He concentrations in the centre  
745 of the modelled grains with radii >40 µm, is nearly unaffected by the high radionuclide  
concentration in the rim of the grain (e.g., Fig. 13A,G). In this specific scenario, modelling  
in-situ (U-Th-Sm)/He data from the centre of grains correctly retrieves the cooling assuming  
constant radionuclide concentration of 10 ppm (Fig. 13I,J). Instead, using the mean whole-  
grain radionuclide concentration as input results in incorrect cooling histories (Fig. 13K,L).  
750 We modelled whole-grain (U-Th-Sm)/He data to investigate the ability to reconstruct the  
input thermal history of zoned grains. Modelled whole grain (U-Th-Sm)/He are between 57.3  
Ma, 58.7 Ma and 59.0 Ma for grains with 40, 80 and 100 µm grain radius and rapid cooling

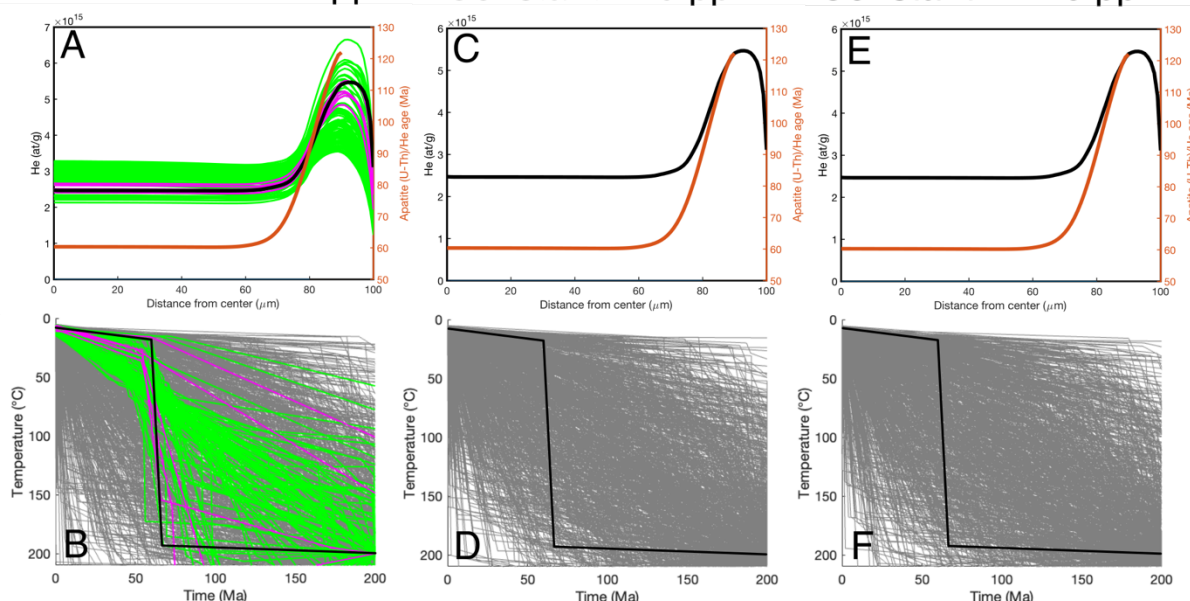
to the surface temperature at 60 Ma. The whole-grain data can retrieve the general cooling trend in case the radionuclide distribution is precisely known (Fig. 13M). The latter, however, 755 is commonly not measured, and instead, the whole-grain average radionuclide concentration is measured and used for thermal history modelling. Interestingly, the modelling does not retrieve the correct or any acceptable cooling history (Fig. 13O), which we interpret as a result of incorrect He diffusivities associated with the assumption of homogenous inter-grain variable radionuclide concentrations (19.4 vs. 27.5 ppm). For comparison, we also modelled 760 the thermal history using a radionuclide concentration of 10 ppm for both grains (Fig. 13N). Although acceptable and good thermal paths are predicted by inverse modelling, the correct input thermal history could not be retrieved.

## Single-grain approach

Core/Rim - 10/50 ppm

Constant - 10 ppm

Constant - 17.6 ppm

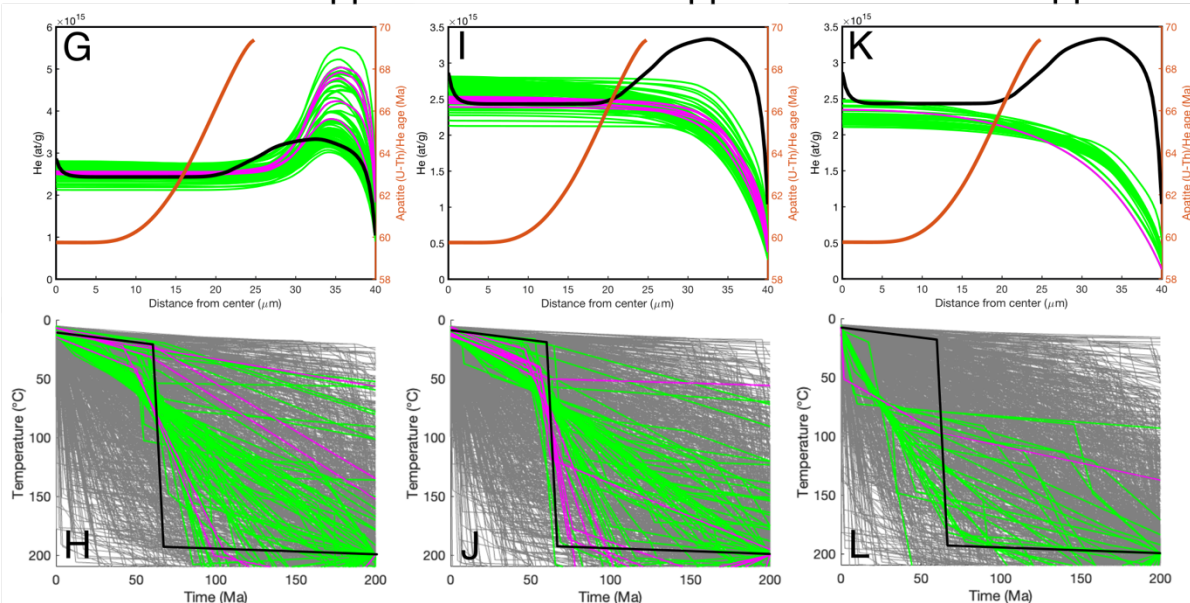


## Multi-grain approach

Core/Rim - 10/50 ppm

Constant - 10 ppm

Constant - 19.4/27.5 ppm



## Whole-grain approach

Core/Rim - 10/50 ppm

Constant - 10 ppm

Constant - 19.4/27.5 ppm

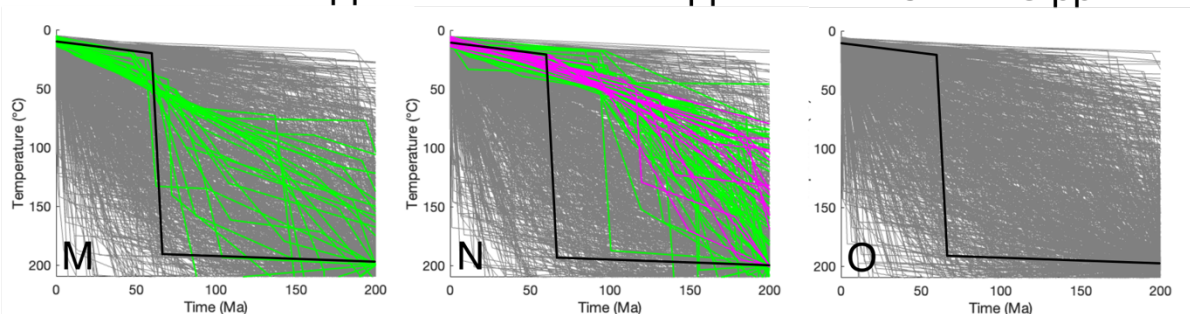


Fig. 13: Cooling histories predicted from in-situ and whole-grain (U-Th-Sm)/He  
765 measurements of a synthetic cylindrical apatite grain with a radius of 40, 80 and 100  $\mu\text{m}$ , and  
U, Th, and Sm concentrations of 10 ppm in the core and 50 ppm in the 10  $\mu\text{m}$  wide rim. All  
input data is modelled with fast cooling to surface temperature at 60 Ma. Retrieving the  
thermal history assumes either (i) precise knowledge of the radionuclide variation and  
distribution (left column), (ii) a homogenous radionuclide concentration of 10 ppm (middle  
770 column) and (iii) whole-grain average homogenous radionuclide concentration (right  
column). A-F) Single-grain approach with five 20  $\mu\text{m}$  diameter (5  $\mu\text{m}$  depth) ablation pits  
across a grain with 100  $\mu\text{m}$  radius are used as synthetic input data. Upper panels (A,C,E) do  
show synthetic (black line) and modelled (green, magenta) He profiles, while the brown line  
represents the in-situ (U-Th-Sm)/He dates. The lower panels (B,D,F) show the input (black)  
775 and modelled (gray, green, magenta) cooling paths. Predicted cooling histories with  
acceptable paths are green (GOF>0.05), good paths are magenta (GOF>0.5), and paths with a  
GOF<0.05 are grey. G-L) Multi-grain approach using a central 30  $\mu\text{m}$  diameter (5  $\mu\text{m}$  depth)  
ablation pit in two grains (40 and 80  $\mu\text{m}$  radii) as synthetic input data. G-L) Similar to A-F  
but for a multi-grain approach. M-O) Thermal inversion results for two grains with 40 and 80  
780  $\mu\text{m}$  radii using the whole-grain approach.

## 4.0 Discussion

### 785 4.1 Synthesis of results

The previous results suggest that in-situ (U-Th-Sm)/He dating can provide an improvement in  
date and thermal history calculation compared to the conventional whole-grain analyses. This  
is due to the technique's capability to detect for radionuclide zoning, thereby resulting in  
790 reliable date predictions and thermal history reconstructions. The latter, however, can be only  
achieved when grains with radionuclide zoning are excluded, since accounting for zoning  
would ideally require a 3D mapping and modelling approach which is not routinely feasible.  
However, a caveat of the in-situ approach is that individual spot dates will be variable across  
the grain even without radionuclide zoning, and a framework is required for interpreting  
795 them.

Based on the previous analysis, we suggest two different measurement approaches for in-situ  
(U-Th-Sm)/He dates to yield geologically relevant data. These approaches include single-spot

measurements from multiple grains from a single sample and multiple spot locations across a single grain. In both cases, potential inner-grain radionuclide variations need to be studied, for instance, making maps, line scans or drilling through the whole grain with a LA-ICP-MS system. In addition, a combination of both single- and multiple-spot approaches might be practical, with single-spot measurements in small grains and multiple spots in larger grains. Anyway, the resulting dates can be used to reconstruct the sample's cooling history for cooling rates between 1-40 °C/Myr. Faster cooling rates (e.g., 100 °C/Myr) characteristic of rapidly exhuming orogens (e.g., Himalaya, Taiwan, New Zealand) were not explored in this study and may present additional challenges if parent radionuclide concentrations are low (e.g., 1-10 ppm) leading to low He concentrations that are below the detection limit using reasonable pit diameters ( $\ll 100 \mu\text{m}$ ).

Results presented here were based on simulated ablation pit diameters of 20 and 30  $\mu\text{m}$  (5  $\mu\text{m}$  deep) and U, Th, and Sm concentrations of 10 ppm. With these values, in-situ dating of apatite grains as young as ~60 Ma and analytical uncertainty of ~10% is possible (with our measurement limit of detection being 0.000079 ncc He). Accordingly, ages as young as 10 Ma can be measured with a pit diameter of 30  $\mu\text{m}$  (10  $\mu\text{m}$  deep). Increasing the pit volume further would be problematic for deriving the cooling history from in-situ (U-Th-Sm)/He data, especially if grains are small. Larger pit volumes integrate more likely areas of the grain affected by He ejection and limit the number of pits placed in a single grain. Given these factors, we recommend that future investigations of in-situ analytical procedures analyse large grains and measure He in as small as detectable pit volumes for reconstructing thermal histories.

820

#### 4.2 Meaning of in-situ dates

Whole-grain (U-Th-Sm)/He dates primarily depend on the sample cooling history and, to a lesser degree vary with grain size, radionuclide concentration and the alpha-damage density. In addition, they can occasionally be biased by radionuclide zoning or inclusions (e.g., Farley, 2002). In the rare case of rapid cooling to surface temperatures, the whole-grain date (irrespective of grain size and radionuclide concentration) reflects the time of that cooling event (e.g., Wolf et al., 1998). Importantly, the same date can be reproduced by slow monotonic cooling and even cooling followed by reheating (e.g. Wolf et al., 1998). In the latter case, the (U-Th-Sm)/He date might even correspond to the time when the sample was at the surface temperature. A single whole-grain (U-Th-Sm)/He date alone does not hold much

830

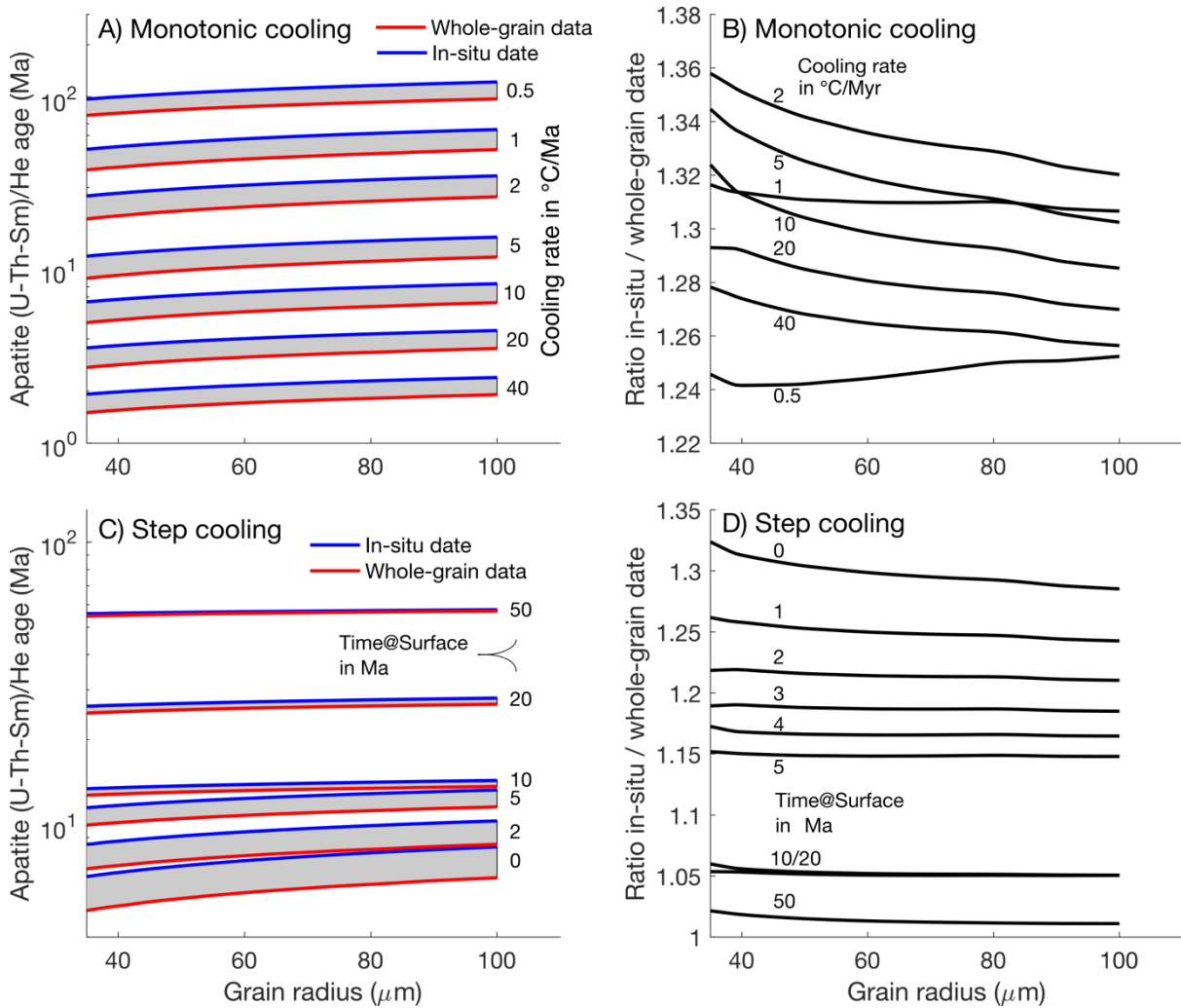


information on the thermal history, which requires analysis of more grains or a joint interpretation with other thermochronology methods and geological constraints.

835 Our modelling in-situ and whole-grain (U-Th-Sm)/He dates for slow to fast cooling rates (1-40°C/Myr) indicates that dates are commonly older than the corresponding whole-grain date for monotonic cooling (Fig. 8). In a study with a larger variation in parameters, we explored the relationship between whole-grain and in-situ dates for very slow to fast cooling rates (0.5-40°C/Myr) in more detail (Fig. 14). Monotonic cooling, irrespective of the cooling rate, results in roughly 30% older in-situ dates compared to whole-grain dates (Fig. 14A,B).

840 Cooling with a rate of 10°C/Myr to a surface temperature of 10°C at different times results in variable differences in whole-grain vs. in-situ dates (Fig. 14C-D). Dates are nearly identical for cooling to surface temperature at 50 Ma, and dates diverge for cooling histories to surface temperatures at younger times.

The fundamental difference between whole-grain and in-situ (U-Th-Sm)/He dating is the  
845 location and volume where He is measured in a grain, whereas the differences in dates between the methods strongly depend on the cooling history and associated diffusion history. He production and ejection result in strong concentration differences in grains, which set the pace for diffusional He loss increasing from the centre to the rim of a grain, as illustrated with our modelled He profiles (e.g. Fig. 12). Measuring He in the centre of grains, as is common  
850 practice in in-situ dating, leads to older ages than whole-grain dating. The latter includes diffusion-related He-depleted grain rims, yielding younger dates. Samples where the majority of produced He has not been affected by high diffusion rates have similar whole-grain and in-situ dates, such as in the rapidly cooled Fish Canyon age standard (e.g. Horne et al., 2016; Pickering et al., 2020) or Ellendale pipe samples (Evans et al., 2015). In one additional  
855 scenario, whole-grain and in-situ dates are anticipated to exhibit identical dates. This occurs with very-large crystals irrespective of their specific cooling history, exemplified by Durango apatite and Madagascar monazite and zircon (see Boyce et al., 2006; Evans et al., 2015; Horne et al., 2019; Vermeesch et al., 2012).



860 Fig. 14: Whole-grain vs. in-situ (U-Th-Sm)/He dates as a function of grain size and cooling rate for a U, Th, and Sm concentration of 10 ppm (homogenously distributed) and assuming a single spot radius of 10  $\mu\text{m}$  (2  $\mu\text{m}$  deep) in the centre of a spherical grain. A) Dates for cooling rates of 0.5 to 40  $^{\circ}\text{C}/\text{Myr}$ . B) Ratio of in-situ and whole-grain dates as a function of grain size and cooling rate. C-D) Same as A and B, but modelled with a step cooling to surface temperature (10 $^{\circ}\text{C}$ ) at different times (0-50 Ma) with a cooling rate of 10 $^{\circ}\text{C}/\text{Myr}$ .  
865

Tripathy-Lang et al. (2013) applying the in-situ method to detrital zircons from a tributary of the Indus River in the Himalayas, draining the southern part of the Ladakh batholith, with the in-situ method. Cooling of the Ladakh batholith through the He partial retention zone for zircons likely occurred rapidly in Oligocene times (Kirstein et al., 2009). According to our modelling results, this should result in similar whole-grain and in-situ zircon dates. In fact, the resulting whole-grain and in-situ date distributions show comparable patterns, with slightly older whole-grain dates (mean date 29 vs. 26 Ma). Tripathy-Lang et al. (2013)  
870

875 interpreted the difference to result from preferential grain selection for whole-grain analyses  
and considered the in-situ dates to be more representative. Alternatively, the larger spread  
and slight shift to older dates may be based on methodological differences, where in-situ  
dates are generally older for samples that have experienced diffusional He loss.  
In summary, in-situ (U-Th-Sm)/He dating of apatite/zircon is an alternative to whole-grain  
880 dating with obvious advantages. However, our modelling results demonstrate that dates  
cannot simply be interpreted together with whole-grain data. If analysed grains are expected  
to have lost a significant fraction of He by diffusion, in-situ dates will be older than whole-  
grain dates. In the case of bedrock studies, in-situ data can be interpreted using modified  
thermal models introduced here, and to aid comparisons to existing whole-grain datasets,  
885 corresponding whole-grain data can be derived from those models. In most detrital studies, it  
is impossible to know the fractional loss of He of each individual grain and in-situ dates, if  
measured in the centre of grains, will be systematically older. In case the dates of source  
areas are largely different (e.g., 15 vs. 30 vs. 90 Ma), inferences from in-situ (U-Th-Sm)/He  
dating might still be acceptable, such as the detrital zircon study from the Inn River in the  
890 European Alps by Dunkl et al. (2024).

#### 4.3 Grain selection considerations for in-situ measurement

895 Grain selection for the in-situ (U-Th-Sm)/He method follows criteria similar to the whole-  
grain method. Simple 1D thermal history modelling requires that selected grains have smooth  
surfaces and are symmetrical, such as spheres and cylinders. The long-prismatic shape and  
basal cleavage direction often result in the fragmentation of apatite grains, especially during  
the mineral separation process (e.g., Farley, 2002). Interpreting apatite fragments with the  
900 whole-grain and  $^4\text{He}/^3\text{He}$  method usually requires corrections for grain fragmentation (e.g.,  
Brown et al., 2013; Flowers and Farley, 2012). Instead, fragments of apatite grains broken  
along the basal faces can be treated similarly to intact grains with the in-situ (U-Th-Sm)/He  
method.

Grains should be free of inclusions to avoid excess He from long-alpha stopping distances  
905 (e.g., Farley, 2002). The pre-measurement exposure of the inner surface facilitates thorough  
inspection of the grain interior and identification of potential inclusions at sub- $\mu\text{m}$  resolution  
using 1000x magnification. Even though not visually evident with microscopy, inclusions can  
be identified by measuring radionuclide concentrations with LA-ICP-MS. The downside of

analyzing inner surfaces after abrasion is that roughly half of the grain is not available for  
910 inspection, and thus outliers related to excess He from mineral inclusions (abraded away) will  
still be an issue in in-situ (U-Th-Sm)/He dating.

Similar to the whole-grain method, reliable date determination and thermal history  
reconstructions require precise measurements of grain geometries (e.g., Glotzbach et al.,  
2019). Future applications of the in-situ (U-Th-Sm)/He methodology will show if geometry  
915 measurements are required before embedding grains, or measurements can be done within the  
mount following grain selection. Measurements of the distance between He laser pits and  
grain prism faces can follow pit volume measurements. An issue that may arise is the  
complexity involved in accurately determining the position of the inner surface relative to the  
original grain boundary, particularly in the vertical dimension of mounted grains. The  
920 common tetragonal and hexagonal cross-sectional shapes of zircons and apatites result in  
theoretically variable-sized inner surfaces (e.g. Fig. 7). A symmetrical apatite and simple  
zircon grain have a ratio between circum- to inner radius of 1/1.15 and 1/1.41, respectively. It  
is, therefore, mandatory to accurately determine the correct location of the pit location with  
respect to the whole-grain geometry.

925

#### 4.4 Recommended reporting procedure for in-situ analytical data.

We recommend using the 1D modelling approach only for grains with homogeneous or  
concentric radionuclide distribution. The latter should be verified by spatial-/depth-resolved  
930 radionuclide information, e.g., with LA-ICP-MS depth profiling or mapping. Based on the  
model results presented here and the discussion in the previous section, we recommend  
reporting several different aspects of in-situ measurements. These items will enable not only  
reproduction of dates for each spot, but also facilitate modelling of grain thermal histories  
using the software of this study. Essential items to report in data tables for each grain include:  
935 1) grain geometry (preferably with photos in a supplement) and assumed grain geometry  
(e.g., sphere, infinite cylinder, other) used for age calculation, 2) (for each ablation pit across  
a grain) the pit diameter, measured volume, depth, and center point of the pit relative to the a-  
, b- and c-axis of the grain, 3) the He measured from the ablation pit, 4) the U, Th and Sm  
concentration profiles, 5) the calculated in-situ grain date, and 6) the whole-grain equivalent  
940 date (which requires thermal history modelling, see Fig. 14). Reporting of the above  
information enables thermal history modelling of individual grains and comparison of in-situ  
dates to whole-grain dates from neighbouring areas and/or previous studies.

#### 4.5 Future considerations

945

Although the theoretical benefits and limitations have been explored here, more applications of the in-situ (U-Th-Sm)/He method to samples are required. Future studies should explore (i) the spatial relationship between radionuclide zoning and resulting He distribution, and (ii) the reliability of in-situ (U-Th-Sm)/He-derived thermal history reconstructions. Lastly (iii), as previously mentioned, future modelling studies should evaluate tradeoffs between the cooling rate (particularly at higher cooling rates of  $>10$  °C/Myr) and parent radionuclide concentrations to evaluate the limits of in-situ dating to produce geologically interpretable data.

950

955

#### 5.0 Conclusions

This study examined the theoretical relationship between the parent radionuclide distribution and the resulting He concentrations within a grain (such as apatite or zircon). This was done using an updated version of the production, ejection, and diffusion model (i.e., RDAAM). We investigated the dependencies of predicted whole-grain and in-situ apatite and zircon (U-Th-Sm)/He dates for monotonic cooling histories (1-40 °C/Myr), grain size (40-100  $\mu\text{m}$ ), and (in the case of in-situ data) the position of the measurement within the grain. In addition, we explored strategies for reconstructing the thermal history from multiple and single apatite grains.

960

965

Model predictions revealed that the He concentration and resulting in-situ date is mainly a function of the grain size, eU, and distance to the grain rim. Thus, the interpretation of in-situ (U-Th-Sm)/He dates necessitates the assessment of the grain geometry of the measured grains and determining the distance between the laser spot and the closest prismatic face. Most importantly, in-situ dates for samples that experienced diffusional He loss will be older than whole-grain dates. In most cases, understanding in-situ data necessitates the application of adapted thermal models such as those introduced in this study. Additionally, to facilitate a comparison to existing whole-grain data, corresponding whole-grain dates can be determined through thermal history modelling.

970

975

Our observations revealed that radionuclide zoning is not an anomaly but a prevalent occurrence in both apatite and zircon. Analysis of a substantial dataset using LA-ICP-MS for

radionuclide measurements in these minerals demonstrated that the observed radionuclide zoning has, if disregarded, the potential to substantially skew the relationships between effective uranium (eU) and whole-grain dates. Furthermore, results suggest that a minimum  
980 of 10 apatite grains are needed to reach an  $R^2$  of 0.8 between eU and date and a labour-intensive number (23) of whole-grain ZHe dates is needed to reach a minimum  $R^2$  of 0.5 between eU and date.

Two promising approaches exist for reconstructing the thermal history of rocks using the in-situ (U-Th-Sm)/He method. Similar to data obtained from whole grains, variations in grain  
985 size and/or effective uranium content, which lead to differences in helium diffusivity and in-situ dates, can be utilized for thermal history reconstructions. The in-situ (U-Th-Sm)/He method can measure a He concentration profile in single grains, which is, among other factors, controlled by the cooling history. Modelling results suggest that several in-situ (U-Th-Sm)/He measurements along a profile from the centre of a grain to the prism face can be  
990 inverted to reconstruct the thermal history of a single grain.

#### **Author contribution**

Conceptualization: CG, TE

Formal analysis: CG

995 Investigation: CG

Methodology: CG

Software: CG

Visualization: CG

Writing: CG, TE

1000

#### **Code availability**

The modified version of RDAAM and ZRDAAM code and Matlab scripts to run these models are available from the Zenodo repository (<https://doi.org/10.5281/zenodo.13898183>).

1005

#### **Competing interests**

The contact author has declared that none of the authors has any competing interests.

#### **Acknowledgements**

1010 This study was supported by (1) the Deutsche Forschungsgemeinschaft (DFG) to Christoph  
Glotzbach (GL 724/11-1) under the priority program 4D-MB and is a contribution to the  
AlpArray initiative, (2) the Bundesgesellschaft für Endlagerung (BGE – STAFuE-21-12-  
Klei), and (3) a large equipment funding by the DFG to Todd Ehlers (INST 37/1041-1  
FUGG). The manuscript benefitted from discussions with Sarah Falkowski and Ann-Kathrin  
1015 Maier, and improved through the thoughtful reviews of Istvan Dunkl, Rebecca Flowers and  
comments from the associate editor Pieter Vermeesch. Klaus Metzger is thanked for editorial  
handling and technical corrections.

## 6.0 References Cited

- 1020 Anderson, A. J., Hodges, K. V., and van Soest, M. C.: Empirical constraints on the effects of  
radiation damage on helium diffusion in zircon, *Geochimica et Cosmochimica Acta*,  
218, 308–322, <https://doi.org/10.1016/j.gca.2017.09.006>, 2017.
- Bragg, W. H., and Kleeman, R.: On the  $\alpha$  particles of radium, and their loss of range in  
1025 passing through various atoms and molecules. *The London, Edinburgh, and Dublin  
Philosophical Magazine and Journal of Science*, 10(57), 318–340,  
<https://doi.org/10.1080/14786440509463378>, 1905.
- Boyce, J. W., Hodges, K. V., Olszewski, W. J., Jercinovic, M. J., Carpenter, B. D., &  
Reiners, P. W. (2006). Laser microprobe (U–Th)/He geochronology. *Geochimica et*  
1030 *Cosmochimica Acta*, 70(12), 3031–3039. <https://doi.org/10.1016/j.gca.2006.03.019>
- Brown, R. W., Beucher, R., Roper, S., Persano, C., Stuart, F., & Fitzgerald, P. (2013).  
Natural age dispersion arising from the analysis of broken crystals. Part I: Theoretical  
basis and implications for the apatite (U–Th)/He thermochronometer. *Geochimica et*  
*Cosmochimica Acta*, 122, 478–497. <https://doi.org/10.1016/j.gca.2013.05.041>
- 1035 Chew, D. M., Petrus, J. A., Kenny, G. G., & McEvoy, N. (2017). Rapid high-resolution U–Pb  
LA-Q-ICPMS age mapping of zircon. *Journal of Analytical Atomic Spectrometry*,  
32(2), 262–276. <https://doi.org/10.1039/C6JA00404K>
- Dunkl, I., Malis, F., Lünsdorf, N. K., Schönig, J., & Von Eynatten, H. (2024). Zircon U-Pb-  
He Double Dating of Modern Sands From the Inn River Catchment: Assessing  
1040 Resolution and Potential in a Complex Orogenic Setting. *Journal of Geophysical  
Research: Earth Surface*, 129(1), e2023JF007360.  
<https://doi.org/10.1029/2023JF007360>

- Ehlers, T. A.: Crustal Thermal Processes and the Interpretation of Thermochronometer Data, *Reviews in Mineralogy and Geochemistry*, 58(1), 315–350,  
1045 <https://doi.org/10.2138/rmg.2005.58.12>, 2005.
- Ehlers, T. A. and Farley, K. A.: Apatite (U–Th)/He thermochronometry: methods and applications to problems in tectonic and surface processes, *Earth and Planetary Science Letters*, 206, 1–14, [https://doi.org/10.1016/S0012-821X\(02\)01069-5](https://doi.org/10.1016/S0012-821X(02)01069-5), 2003.
- Evans, N. J., McInnes, B. I. A., McDonald, B., Danišik, M., Becker, T., Vermeesch, P., et al.  
1050 (2015). An *in situ* technique for (U–Th–Sm)/He and U–Pb double dating. *J. Anal. At. Spectrom.*, 30(7), 1636–1645. <https://doi.org/10.1039/C5JA00085H>
- Danišik, M., McInnes, B. I. A., Kirkland, C. L., McDonald, B. J., Evans, N. J., and Becker, T.: Seeing is believing: Visualization of He distribution in zircon and implications for thermal history reconstruction on single crystals, *Science Advances*, 3(2), e1601121,  
1055 <https://doi.org/10.1126/sciadv.1601121>, 2017.
- Falkowski, S., Ehlers, T. A., McQuarrie, N., Glover, C. O., Perez, N. D., and Buford Parks, V. M.: Exhumation and incision of the eastern Central Andes, southern Peru: Low-temperature thermochronology observations, *Earth and Planetary Science Letters*, 620, 118299, <https://doi.org/10.1016/j.epsl.2023.118299>, 2023.
- 1060 Farley, K. A., Wolf, R. A., and Silver, L. T.: The effects of long alpha-stopping distances on (U–Th–Sm)/He dates, *Geochimica et Cosmochimica Acta*, 60(21), 4223–4229, [https://doi.org/10.1016/s0016-7037\(96\)00193-7](https://doi.org/10.1016/s0016-7037(96)00193-7), 1996.
- Farley, K. A.: Helium diffusion from apatite: General behavior as illustrated by Durango fluorapatite, *Journal of Geophysical Research: Solid Earth*, 105(B2), 2903–2914,  
1065 <https://doi.org/10.1029/1999JB900348>, 2000.
- Farley, K. A.: (U–Th–Sm)/He Dating: Techniques, Calibrations, and Applications, *Reviews in Mineralogy and Geochemistry*, 47(1), 819–844, <https://doi.org/10.2138/rmg.2002.47.18>, 2002.
- 1070 Farley, K. A., Shuster, D. L., Watson, E. B., Wanser, K. H., and Balco, G.: Numerical investigations of apatite  $^4\text{He}/^3\text{He}$  thermochronometry: APATITE  $^4\text{He}/^3\text{He}$  THERMOCHRONOMETRY, *Geochemistry, Geophysics, Geosystems*, 11(10), <https://doi.org/10.1029/2010GC003243>, 2010.
- Farley, K. A., Shuster, D. L., and Ketcham, R. A.: U and Th zonation in apatite observed by laser ablation ICPMS, and implications for the (U–Th)/He system, *Geochimica et Cosmochimica Acta*, 75(16), 4515–4530, <https://doi.org/10.1016/j.gca.2011.05.020>,  
1075 2011.



- Flowers, R. M.: Exploiting radiation damage control on apatite (U–Th)/He dates in cratonic regions, *Earth and Planetary Science Letters*, 277(1–2), 148–155, <https://doi.org/10.1016/j.epsl.2008.10.005>, 2009.
- 1080 Flowers, R. M., Ketcham, R. A., Shuster, D. L., and Farley, K. A.: Apatite (U–Th)/He thermochronometry using a radiation damage accumulation and annealing model, *Geochimica et Cosmochimica Acta*, 73(8), 2347–2365, <https://doi.org/10.1016/j.gca.2009.01.015>, 2009.
- Flowers, R. M., & Farley, K. A. (2012). Apatite  $4\text{He}/3\text{He}$  and (U–Th)/He Evidence for an  
1085 Ancient Grand Canyon. *Science*, 338(6114), 1616–1619. <https://doi.org/10.1126/science.1229390>
- Flowers, R. M., Ketcham, R. A., Enkelmann, E., Gautheron, C., Reiners, P. W., Metcalf, J. R., et al. (2023). (U–Th)/He chronology: Part 2. Considerations for evaluating, integrating, and interpreting conventional individual aliquot data. *GSA Bulletin*, 135(1–  
1090 2), 137–161. <https://doi.org/10.1130/B36268.1>
- Fox, M., McKeon, R. E., and Shuster, D. L.: Incorporating 3-D parent nuclide zonation for apatite  $^4\text{He}/^3\text{He}$  thermochronometry: An example from the Appalachian Mountains, *Geochemistry, Geophysics, Geosystems*, 15(11), 4217–4229, <https://doi.org/10.1002/2014GC005464>, 2014.
- 1095 Fox, M., Tripathy-Lang, A., & Shuster, D. L. (2017). Improved spatial resolution of elemental maps through inversion of LA-ICP-MS data. *Chemical Geology*, 467, 30–41. <https://doi.org/10.1016/j.chemgeo.2017.07.001>
- Gallagher, K., Brown, R., and Johnson, C.: Fission track analysis and its applications to geological problems, *Annual Review of Earth and Planetary Sciences*, 26(1), 519–572,   
1100 <https://doi.org/10.1146/annurev.earth.26.1.519>, 1998.
- Gautheron, C., Tassan-Got, L., Barbarand, J., and Pagel, M.: Effect of alpha-damage annealing on apatite (U–Th)/He thermochronology, *Chemical Geology*, 266(3–4), 157–170, <https://doi.org/10.1016/j.chemgeo.2009.06.001>, 2009.
- Glotzbach, C., Lang, K. A., Avdievitch, N. N., and Ehlers, T. A.: Increasing the accuracy of  
1105 (U–Th(-Sm))/He dating with 3D grain modelling, *Chemical Geology*, 506, 113–125, <https://doi.org/10.1016/j.chemgeo.2018.12.032>, 2019.
- Guenther, W. R., Reiners, P. W., Ketcham, R. A., Nasdala, L., and Giester, G.: Helium diffusion in natural zircon: Radiation damage, anisotropy, and the interpretation of zircon (U–Th–Sm)/He thermochronology, *American Journal of Science*, 313(3), 145–  
1110 198, <https://doi.org/10.2475/03.2013.01>, 2013.

- Guenther, W. R., Reiners, P. W., Drake, H., and Tillberg, M.: Zircon, titanite, and apatite (U-Th-Sm)/He dates and date-eU correlations from the Fennoscandian Shield, southern Sweden: Fennoscandian Zirc He Date-eU Correlation, *Tectonics*, 36(7), 1254–1274, <https://doi.org/10.1002/2017TC004525>, 2017.
- 1115 Horne, A. M., van Soest, M. C., Hodges, K. V., Tripathy-Lang, A., and Hourigan, J. K.: Integrated single crystal laser ablation U/Pb and (U–Th)/He dating of detrital accessory minerals – Proof-of-concept studies of titanites and zircons from the Fish Canyon tuff, *Geochimica et Cosmochimica Acta*, 178, 106–123, <https://doi.org/10.1016/j.gca.2015.11.044>, 2016.
- 1120 Horne, A. M., van Soest, M. C., and Hodges, K. V.: U/Pb and (U-Th-Sm)/He “double” dating of detrital apatite by laser ablation: A critical evaluation, *Chemical Geology*, 506, 40–50, <https://doi.org/10.1016/j.chemgeo.2018.12.004>, 2019.
- Hourigan, J. K., Reiners, P. W., and Brandon, M. T.: U-Th zonation-dependent alpha-ejection in (U-Th)/He chronometry, *Geochimica et Cosmochimica Acta*, 69, 3349–3365, <https://doi.org/10.1016/j.gca.2005.01.024>, 2005.
- 1125 Ketchum, R. A.: Forward and Inverse Modeling of Low-Temperature Thermochronometry Data. *Reviews in Mineralogy and Geochemistry*, 58(1), 275–314, <https://doi.org/10.2138/rmg.2005.58.11>, 2005.
- [Ketchum, R. A., Gautheron, C., & Tassan-Got, L. \(2011\). Accounting for long alpha-particle stopping distances in \(U–Th–Sm\)/He geochronology: Refinement of the baseline case. \*Geochimica et Cosmochimica Acta\*, 75\(24\), 7779–7791. <https://doi.org/10.1016/j.gca.2011.10.011>](https://doi.org/10.1016/j.gca.2011.10.011)
- 1130 Kirstein, L. A., Foeken, J. P. T., van der Beek, P., Stuart, F. M., and Phillips, R. J.: Cenozoic unroofing history of the Ladakh Batholith, western Himalaya, constrained by thermochronology and numerical modelling, *Journal of the Geological Society*, 166, 667–678, <https://doi.org/10.1144/0016-76492008-107>, 2009.
- 1135 Lippolt, H. J., Leitz, M., Wernicke, R. S., and Hagedorn, B.: (Uranium + thorium)/helium dating of apatite: experience with samples from different geochemical environments, *Chemical Geology*, 112(1–2), 179–191, [https://doi.org/10.1016/0009-2541\(94\)90113-9](https://doi.org/10.1016/0009-2541(94)90113-9), 1994.
- 1140 Malusà, M. G., and Fitzgerald, P. G. (Ed.): Fission-track thermochronology and its application to geology. Springer, 393 p, <https://doi.org/10.1007/978-3-319-89421-8>, 2019.

- 1145 Meesters, A. G. C. A., and Dunai, T. J.: Solving the production–diffusion equation for finite diffusion domains of various shapes, *Chemical Geology*, 186(3–4), 333–344, [https://doi.org/10.1016/S0009-2541\(01\)00422-3](https://doi.org/10.1016/S0009-2541(01)00422-3), 2002.
- Pickering, J., Matthews, W., Enkelmann, E., Guest, B., Sykes, C., and Koblinger, B. M.: Laser ablation (U–Th–Sm)/He dating of detrital apatite, *Chemical Geology*, 548, 119683, <https://doi.org/10.1016/j.chemgeo.2020.119683>, 2020.
- 1150 Reiners, P. W.: Zircon (U–Th–Sm)/He Thermochronometry, *Reviews in Mineralogy and Geochemistry*, 58(1), 151–179, <https://doi.org/10.2138/rmg.2005.58.6>, 2005.
- Reiners, P. W. and Ehlers, T. A.: Low-temperature thermochronology: Techniques, interpretations and applications, *Reviews in Mineralogy and Geochemistry*, 58(1), <https://doi.org/10.2138/rmg.2005.58.0>, 2005.
- 1155 Reiners, P. W., and Brandon, M. T.: Using thermochronology to understand orogenic erosion, *Annu. Rev. Earth Planet. Sci.*, 34, 419–466, <https://doi.org/10.1146/annurev.earth.34.031405.125202>, 2006.
- Shuster, D. L., and Farley, K. A.:  $4\text{He}/3\text{He}$  thermochronometry, *Earth and Planetary Science Letters*, 217(1–2), 1–17, [https://doi.org/10.1016/S0012-821X\(03\)00595-8](https://doi.org/10.1016/S0012-821X(03)00595-8), 2004.
- 1160 Spiegel, C., Kohn, B., Belton, D., Berner, Z., and Gleadow, A.: Apatite (U–Th–Sm)/He thermochronology of rapidly cooled samples: The effect of He implantation, *Earth and Planetary Science Letters*, 285(1–2), 105–114, <https://doi.org/10.1016/j.epsl.2009.05.045>, 2009.
- Tripathy-Lang, A., Hodges, K. V., Monteleone, B. D., & van Soest, M. C. (2013). Laser (U–Th)/He thermochronology of detrital zircons as a tool for studying surface processes in modern catchments. *Journal of Geophysical Research: Earth Surface*, 118(3), 1333–1341. <https://doi.org/10.1002/jgrf.20091>
- 1165 Vermeesch, P., Seward, D., Latkoczy, C., Wipf, M., Günther, D., and Baur, H.:  $\alpha$ -Emitting mineral inclusions in apatite, their effect on (U–Th)/He dates, and how to reduce it, *Geochimica et Cosmochimica Acta*, 71(7), 1737–1746, <https://doi.org/10.1016/j.gca.2006.09.020>, 2007.
- 1170 Vermeesch, P., Sherlock, S. C., Roberts, N. M. W., & Carter, A. (2012). A simple method for in-situ U–Th–He dating. *Geochimica et Cosmochimica Acta*, 79, 140–147. <https://doi.org/10.1016/j.gca.2011.11.042>
- 1175 Wolf, R. A., Farley, K. A., and Silver, L. T.: Helium diffusion and low-temperature thermochronometry of apatite, *Geochimica et Cosmochimica Acta*, 60(21), 4231–4240, [https://doi.org/10.1016/s0016-7037\(96\)00192-5](https://doi.org/10.1016/s0016-7037(96)00192-5), 1996.

Wolf, R. A., Farley, K. A., & Kass, D. M. (1998). Modeling of the temperature sensitivity of the apatite (U–Th)/He thermochronometer. *Chemical Geology*, 148(1–2), 105–114.

1180

[https://doi.org/10.1016/S0009-2541\(98\)00024-2](https://doi.org/10.1016/S0009-2541(98)00024-2)